The Sensitivity of Convection to Microphysics and Boundary Layer Parameterizations in Hurricanes Harvey and Irma 2017

Dylan Card*

Committee Members: Kristen L. Corbosiero, Brian H. Tang, Robert G. Fovell, Ryan D. Torn

Department of Atmospheric and Environmental Sciences, University at Albany - State University of New York, Albany, New York

**Corresponding author address:* Dylan Card, Department of Atmospheric and Environmental Sciences, University at Albany - State University of New York, Albany, New York

E-mail: dcard@albany.edu

ABSTRACT

Tropical cyclones (TCs) pose a significant threat to life and property, and exhibit many severe weather hazards as they make landfall, such as storm surge, strong winds, flooding rains, and tornadoes. TC convection is associated with nearly all of these hazards, which can extend hundreds of kilometers inland. Thus, understanding the characteristics and organization of convective cells is important to mitigating risk. Observational studies have noted that TC convection tends to organize downshear and that rotating thunderstorms tend to occur in the downshear-right quadrant of the TC. Modeling studies have also shown that convective cells tend to form upshear right and mature as the traverse cyclonically around the TC. Rotating thunderstorms in TCs are strongly influenced by the low-level helicity and convective available potential energy (CAPE), which have been highlighted in numerous modeling studies. The distribution and magnitude of low-level helicity and CAPE can be strongly influenced by microphysics and planetary boundary layer parameterizations in numerical weather prediction.

High-resolution Weather Research and Forecasting (WRF) simulations of hurricanes Harvey and Irma (2017) will investigate the role of microphysics and boundary layer parameterizations in determining the structure and distribution of rotating and non-rotating convection in TCs. Specifically, this project will examine how double- and single-moment microphysics parameterizations as well as local, non-local, and hybrid planetary boundary layer parameterizations impact the distribution, structure, and longevity of convection. The high resolution (1 km) of these simulations will also allow for the investigation of whether boundaries at the TC or sub-TC scale influence convective organization. This study is unique in that it plans to investigate the interactions between microphysics and planetary boundary layer parameterizations on the development, evolution, and structure of both tropical cyclone convection and boundaries during landfall.

1. Introduction

Tropical cyclones (TCs) pose a significant threat to life and property for those living near the coast, exhibiting many different types of severe weather hazards as they make landfall, such as storm surge, strong winds, flooding rains, and tornadoes. Convection in tropical cyclones can contribute to a variety of these hazards. From 1995 to 2016, rotating convection in tropical cyclones directly resulted in 1296 confirmed tornadoes in the United States, accounting for 10–25% of all tornado activity in the coastal states from Louisiana to Maryland (Edwards 2012). Tropical cyclone tornadoes also make up a large amount of the yearly tornado activity in Japan and China (Bai et al. 2019). Roughly 60% of landfalling tropical cyclones in the United States produce at least one tornado and the threat for such tornadoes can persist for up to five days after landfall (McCaul 1991). The risk for these tornadoes can extend 200–500 km from the tropical cyclone center to inland areas typically spared from strong winds and storm surge. The tornadoes associated with tropical cyclones are typically weak with only 14% rated F/EF2 or higher (Schultz and Cecil 2009). Each tropical cyclone also has large variability in the amount of tornadoes reported. Some storms, such as Hurricane Ivan (2004), produce upwards of 118 tornado reports (Edwards 2010), while others result in no tornado reports although sharing similar intensities and landfall locations. The weak and numerous tornadoes in tropical cyclones present a unique operational challenge to forecasters and decision makers as awareness may be relatively low compared to the other threats present in landfalling tropical cyclones (Weiss 1987; McCaul 1991).

The National Weather Service (NWS) preforms service assessments to evaluate forecast performance following significant weather events such as hurricanes, floods, and impactful winter storms. Their assessment of Hurricane Irene (2011) discussed tornado warning false alarm rates of nearly 88%, which is above-average compared to all tornado warnings. It was also found that the high false alarm rates of tropical cyclone tornado warnings damaged the credibility of the NWS (NWS 2012), taking away from other tropical cyclone risks. Martinaitis (2017) found a similar problem when looking at tropical cyclone landfalls from 2008 to 2013 in the United States that produced at least one confirmed tornado and in which at least 10 tornado warnings were issued. Martinaitis (2017) found that of the 1397 tornado warnings issued during the 12 tropical cyclones examined, only 198 tornado warnings verified, leading to an appalling false alarm rate of nearly 86%. In comparison, the national false alarm rate for tornado warnings in the United States have ranged from 80% in 1998 to 69% in 2016 (Fig. 1), which includes tropical cyclone tornado warnings. Brotzge et al. (2011) found that the false alarm rate for non-tropical cyclone tornado warnings from 2000 to 2004 was about 70%. Thus, tornado predication in tropical cyclones remains difficult.

According to the Storm Prediction Center (SPC), 2017 was the fourth most active year for tornado reports in tropical cyclones behind 2008 (third), 2005 (second), and 2004 (first). The two largest tornado producers of the 2017 tropical cyclone season were Hurricane Harvey and Hurricane Irma. Figures 2 and 3 show the locations of tornado reports during these two storms.

Current research, including this study, are focused on the use of high-resolution, convective-resolving models to study the formation, structure, and evolution, of rotating and non-rotating convection within tropical cyclones. A summary of previous observation and modeling studies that examined rotating convection in tropical cyclones, the effects of microphysics and planetary boundary layer parameterizations on numerical weather prediction, and boundaries within tropical cyclones will motivate this study.

2. Literature review

a. Rotating convection in tropical cyclones

Hurricane Danny (1985) was one of the first hurricane supercell environments to be studied comprehensibly because of the 20 long-track supercells and 22 tornadoes reports it spawned (McCaul 1987). McCaul (1987) noted that not only was veering of the low-level wind important, but so were dry air intrusions, which acted to increase convective instability. McCaul (1991) continued this research by creating a climatology of buoyancy and shear in hurricane-spawned tornado environments using all available sounding data near reported tornado cases in the United States from 1948–1986. For the first time, it was documented that the distributions of buoyancy and shear in hurricanes had significant differences from quadrant to quadrant with respect to north, the direction of the large-scale vertical wind shear, and storm motion. The 0–3-km shear and helicity within the right-front quadrant was the most favorable for producing rotating convection and, in fact, these variables are very well correlated with the observed tornado frequency maximum in the right-front quadrant with respect to motion (McCaul 1991). In addition, climotalogical studies suggest that increased low-level shear is often associated with midlatitude tornado occurrences (Markowski et al. 2003).

Edwards (2012) reviewed the climatology, distributions, and environments of tropical cyclone tornadoes. In this review paper, the synoptic, tropical cyclone, and meso-β scales were examined to summarize what influences tropical cyclone tornado and supercell potential on each scale. On the synoptic scale, the predominant driver of tropical cyclone convective (both rotating and non-rotating) development is the enhancement of vertical shear (McCaul 1991; Molinari and Vollaro 2010). This increase in shear is generally attributed to tropical cyclone recurvature because of midlatitude westerlies and baroclinic boundaries. Consistent with Edwards (2012), Verbout et al.

(2007) found that tropical cyclones with relatively high tornado counts were accompanied by larger 500-hPa geopotential height anomalies and stronger height gradients.

Convection at the tropical cyclone scale is predominantly driven by the distributions of buoyancy and shear. Operational experience indicates that it is common for rotating convection to develop offshore and move inland. Some rotating convection weakens as it moves onto the more thermodynamically stable land as low-level (0–3-km) CAPE is about 35% less (Baker et al. 2009), while other convective cells increase mesocyclone intensity and undergo tornadogensis due to the increased helicity from friction (Edwards 2012). On the meso-β (convective) scale, tropical cyclone supercells have been observed to be smaller in vertical and horizontal extent compared to midlatitude supercells (McCaul and Weisman 1996). Eastin and Link (2009) found in observations of Hurricane Ivan (2004) supercells were typically 5–7 km in diameter, compared to non-tropical cyclone supercells which are typically encompass a larger range of 3–12 km in diameter.

On the mesoscale, low-level, baroclinic, convergent boundaries and dry air intrusion can potentially influence the intensity and spatial distribution of tropical cyclone supercells (Edwards and Pietrycha 2006). Dry air ingested into the midlevels has a strong influence on convective structures in tropical cyclones as it can substantially alter the vertical thermodynamic profile enhancing CAPE (McCaul 1987; Vescio et al. 1996; Curtis 2004). Dry slots can lead to the formation of baroclinic boundaries due to differential heating within the tropical cyclone envelope. Relatively cloud-free areas between tropical cyclone rainbands can support a few degrees Celsius of diabatic surface heating (Card 2019). This surface heating can substantially magnify CAPE and yield baroclinic boundaries that may contribute to supercell maintenance (Edwards 2012). Edwards and Pietrycha (2006) argued that most landfalling tropical cyclones are not homogenized with equal tornado potential everywhere, and that boundaries and dry air intrusions may play a role in the clustering of tornadoes. Indeed, tropical cyclone tornado outbreak cases tend to have pronounced relative humidity gradients from 700–500 hPa at the outer edge of the moist tropical cyclone envelope (Curtis 2004)

Of tropical cyclones from 1948 to 2019, Hurricane Ivan (2004) holds the record for the number of tropical cyclone confirmed tornadoes at 118 (McCaul 1991; Schultz and Cecil 2009). Baker et al. (2009) looked at the environmental ingredients for the development of supercells and tornadoes in Hurricane Ivan via airborne and land-based observations. The azimuthal location of the tornadoes in Hurricane Ivan could be explained by significant 0–1-km shear (7.4 $\frac{m}{s}$) and low lifting condensation level (LCL) heights (415 m) in the right-front quadrant with respect to storm motion. Motivated by an apparent increase in individual convective cell rotation as convection made landfall, Baker et al. (2009) further investigated the differences in the convective environments between the sea and land. They found that the land soundings had very similar total-column CAPE to the sea soundings; however, the low-level (0–3-km) CAPE was 35% less over the land. McCaul and Weisman (1996, 2001) suggested that updraft strength and vorticity were both enhanced when buoyancy is concentrated in the low-levels, suggesting convection is more likely to form over the ocean and move onshore. The other appreciable difference between the land and sea environments in Baker et al. (2009) was that the 0–1-km storm relative helicity (SRH) was 50% greater over land, due to frictional effects.

Although not observed in Hurricane Ivan, some researchers have suggested that changes in surface wind speeds as large as 8–10 $\frac{m}{s}$ could occur across horizontal distances of 10 km at land–ocean interfaces (Powell and Houston 1998). Gentry (1983) showed that there is an increase in low-level helicity because of the increase in friction between the land–sea interface acting to enhance low-level vertical shear. As a result, individual convective cells making landfall tend to increase updraft rotation and intensity due to the enhanced low-level shear (Baker et al. 2009).

Eastin and Link (2009) used the same collection of airborne and land-based observations as Baker et al. (2009), and concluded that the offshore environment was conducive for supercell formation. In the examination of the individual rotating convective cells, mesocyclonic updrafts extended from the boundary layer up to 6–8 km and were 5–7 km in diameter. The production of the updraft likely results from a combination of convergence, thermal instability, and perturbation pressure gradients, which help to produce mesocyclones by tilting and stretching environmental vorticity (Eastin and Link 2009).

These observational studies of Hurricane Ivan (2004) led to high-resolution, real-data simulations to document the structure of potentially tornadic supercells embedded within tropical cyclone rainbands. Carroll-Smith et al. (2019) produced one such simulation at 3- and 1-km grid spacing. In an attempt to verify the tropical cyclone tornadoes associated with Hurricane Ivan (2004), percentile values of maximum updraft helicity and simulated radar reflectivity were used to identify tropical cyclone tornado surrogates and compare those surrogates to observed tornado reports. The surrogates with the 99.9^{th} (99.95^{th}) percentile of maximum updraft helicity in the 3-km (1-km) domain provided the most favorable results capturing the distribution of tropical cyclone tornadoes compared to observations. These high updraft helicity percentiles suggest that supercells with strong mesocyclones are more likely to produce tornado reports in tropical cyclones. In this modeling study of Hurricane Ivan, updraft helicity and simulated radar reflectivity were used successfully as tropical cyclone tornado surrogates (Carroll-Smith et al. 2019).

Card (2019) used a similar analysis technique to Carroll-Smith et al. (2019) to diagnose rotating convection in hurricanes Harvey and Irma (2017) using the he National Center for Atmospheric Research (NCAR) 10 member ensemble. In Card (2019), the number of identified rotating storms outnumbered the identified non-rotating storms by a factor of 2–3 in both Harvey and Irma (2017). With respect to storm motion and north the distributions of rotating and non-rotating convection is very similar (Figs. 4 and 5). There is a strong relationship between shear and storm motion near the US coasts because tropical cyclones are typically recurving. As shown in Corbosiero and Molinari (2003), shear is the dominate factor in the distribution of convection in tropical cyclones. Most of the rotating storms occur directly downshear, while most of the non-rotating storms occur upshear-right in both the NCAR ensemble and in observations (Figs. 4 and 5).

In summary, the common environmental characteristics of tornadic rotating convection in tropical cyclones are: 1) high 0–3-km storm relative helicity (SRH), 2) high 0–3-km CAPE, 3) low lifting condensation level (LCL) heights, 4) relatively dry air at midlevels, and 5) low-level boundaries (such as a convergence axis or baroclinic zone) (Novlan and Gray 1974; McCaul 1991; Curtis 2004; Edwards and Pietrycha 2006; Eastin and Link 2009).

b. Microphysics sensitivity in numerical weather prediction

Microphysical schemes parameterize many different small scale processes dealing with precipitation. Microphysics schemes track a number of different species of hydrometers, phase changes, and information about the mass, number, and size of the hydrometers. Single moment microphysics schemes predict the total mass concentration of hydrometers, while double moment microphysics schemes often include a prediction of the total number concentration for some species of hydrometer in addition to mass concentrations. Both the WRF single moment 6-class (WSM6) and the WRF double moment 6-class (WDM6) schemes track the mixing ratios of six different hydrometer species (water vapor, clouds, ice, snow, rain, and graupel) (Hong and Lim 2006; Lim and Hong 2010). WDM6 is double moment for warm rain processes, meaning it additionally provides prognostic number concentrations of cloud and rain water, as well as cloud condensation nuclei (CCN) (Lim and Hong 2010). The predicted CCN number concentration in the WDM6 microphysics scheme adds a level of complexity to traditional bulk microphysics schemes through explicit CCN–cloud drop concentration feedbacks. An example of this is assuming evaporation of cloud drops returns the corresponding CCN particles to the total CCN count. The warm rain source and sink terms are the same for WSM6 and WDM6; however, WDM6 uses auto-conversion and accretion based on Cohard and Pinty (2000). Many of the microphysical processes in WDM6 use the same formulas as WSM6, although they work differently due to the predicted number concentrations of cloud water and rain, which can indirectly influence ice processes (Hong et al. 2010).

Microphysical parameterizations can have a large impact on the vertical structure and development of individual convective cells. It is also well documented in the literature that microphysical parameterization have an impact on tropical cyclone intensity and track (Willoughby et al. 1984; Lord and Lord 1988; Zhu and Zhang 2006; Fovell and Su 2007; Li and Pu 2008; Fovell et al. 2009; Tao et al. 2011; Fovell et al. 2016). The Korean Meteorological Administration (KMA) has used both WSM6 and WDM6 microphysics schemes operationally. The KMA has shown no distinct discrepancies in predicted precipitation between these two schemes, but WDM6 has shown superior predictive skill in a variety of weather conditions (Hong et al. 2010).

The results of Hong et al. (2010) also noted that the WDM6 scheme tends to suppress spurious light precipitation over oceans. Since WDM6 tends to suppress spurious light precipitation that occurs over the ocean, it may affect the degree of clearing seen between rainbands,which can impact the amount of baroclinic forcing and CAPE on the radially inward and outward sides of the rainband convection (Hong et al. 2010; Yussouf et al. 2013). Additional clearing would favor more convectively active rainbands with the possibility of more rotating and non-rotating convective cells.

Hong et al. (2010) also reported that the WDM6 tends to propagate squall-lines too quickly. Distant convective rainbands can sometimes take on squall line-like properties (Houze 2010) and may propagate outward radially too quickly when using the WDM6 microphysics scheme.

Microphysical parameterizations are one important source of error in storm-scale modeling at high resolution. For example, Yussouf et al. (2013) examined a tornadic supercell from 8 May 2003 in Oklahoma City using single and double moment microphysics schemes. The double moment scheme supported a better distribution of the reflectivity in the forward flank region of the simulated supercells than the single moment scheme. Putnam et al. (2017) used 4-km Storm-Scale Ensemble Forecasts (SSEF) to simulate polarmetric radar variables and compared those with observations, specifically looking at the simulation hydrometer types and particle size distributions. Two particular cases, both from 20 May 2013, were examined, the first being a mesoscale convective system and the second being a supercell thunderstorm. Putnam et al. (2017) found that WSM6 had poor coverage of stratiform precipitation. Despite being double-moment for warm rain processes, WDM6 had a similar relationship to WSM6 with respects to simulated reflectivity and differential reflectivity (Putnam et al. 2017). All of the double-moment microphysics schemes tested in Putnam et al. (2017) exhibited incorrect differential refelectivty maxima associated with isolated, weak convection on the back side of the convective lines where large raindrops would not be expected. In both the mesoscale convective system and in the supercell cases, WSM6 produced mainly rain while WDM6 produced mainly rain and graupel. In the supercell case, the WDM6 produced much less reflectivity than the other simulations. They also found that both WSM6 and WDM6 have a bias toward small raindrops and graupel (Putnam et al. 2017).

Numerous studies have highlighted the effects of microphysical parameterizations on tropical cyclones. Fovell et al. (2009) demonstrated that varying microphysics can result in different wind profiles 100–300 km from the storms center, which directly influences the track. Track variations with respect to different microphysics schemes disappear when hydrometeors can no longer interact with longwave and shortwave radiation (Fovell et al. 2010). Tropical cyclone intensity is also influenced by microphysics. In general, the exclusion or reduction in graupel in the cloud results in an increase in intensity and tangential winds in tropical cyclones (McFarquhar et al. 2006; Fovell et al. 2009). Lastly, WDM6 and WSM6 will likely have different cloud, rain, and ice concentrations. Microphysics parameterization produces different concentrations, types, and distributions of hydrometeors which has an impact on storm dynamics and thermodynamics through longwave absorption and emission, and the shortwave absorption (Fovell et al. 2016).

For this experiment the WSM6 and WDM6 microphysics schemes will be compared. In this study, I will examine the sensitivities of tropical cyclone boundaries and rotating convection to single- and double-moment microphysics schemes. Some questions to answer include: How microphysics parameterization affects the distribution, structure, and longevity of rotating and non-rotating convection in tropical cyclones and, do single and double moment microphysics schemes alter how tropical cyclone boundaries form and change over time?

c. Planetary boundary layer sensitivity in numerical weather prediction

The planetary boundary layer (PBL) is customarily divided into two layers, the surface layer (constant-flux layer) and the mixed layer (Kepert 2012). In reality, there is no distinct division between these layers, though the surface layer typically occupies the lowest tenth of the boundary layer. In the WRF model, the surface layer is governed by the surface layer scheme and the mixed layer is governed by the PBL scheme. Because there is no distinct division between these two layers, the PBL scheme must satisfy physics both in the surface and mixed layers depending on the depth of the surface layer in the model. PBL schemes parameterize vertical mixing and diffusion due to eddy mixing in numerical weather models. In most cases, the grid spacing in weather models is not fine enough to resolve turbulent mixing and, therefore, this must be parameterized. There are three major types of PBL schemes: non-local, local, and hybrid.

Non-local schemes use first-order closure allowing for mixing between all the layers in the boundary layer. In this thesis, the Yonsei University (YSU) PBL (Hong et al. 2006) parameterization will be used to represent non-local PBL schemes. The YSU scheme uses K-profile parameterization (KPP). In KPP schemes, the PBL depth plays a crucial role as it can directly influence mixing depth, and the magnitude, and, height of maximum heating (Kepert 2012). The advantages of the YSU scheme are that it can accurately simulate deep vertical mixing in buoyancy driven PBLs and shallower mixing in strong wind environments (Hong and Lim 2006). The PBL heights are determined by where the bulk Richardson number exceeds zero. The YSU scheme tends to overdeepen the PBL in deep convective environments, which often results in too much dry air near the surface (Coniglio et al. 2013). As topical cyclones tend to be moist, this drawback is unlikely.

Local schemes use a higher-order closure than non-local schemes allowing for mixing to only occur between adjacent layers. In this thesis, an improved version of the Mellor–Yamada turbulence closure (MYNN3) model (Nakanishi and Niino 2009) will be used to represent local PBL schemes. Turbulent kinetic energy (TKE) parameterization is used in the MYNN3 scheme. The PBL height is determined by where the TKE falls below a critical value ($1.0 * 10^{-6}\frac{m^2}{s^2}$). MYNN3 uses a second-order closure scheme and can do well at simulating mixed layers and stable boundary layers; however, it has difficulty capturing deep vertical mixing (Nakanishi and Niino 2006). The advantage of the MYNN3 scheme is that it can depict statically stable boundary layers well, which is not particularly advantageous in the environment of a tropical cyclone. Yet, the MYNN3 scheme often does not account fully for deep vertical mixing associated with large eddies or countergradient fluxes, which results in weaker updrafts than observed (Nakanishi and Niino 2006).

Hybrid schemes use a combination of local and non-local mixing to parameterize turbulent motions in the PBL. In this study, the asymmetric convective model version 2 (ACM2) will be used to represent hybrid PBL schemes (Pleim 2007a). ACM2 combines the original non-local ACM with an eddy diffusion such that this scheme uses first-order closure for upward fluxes (much like a non-local PBL schemes would) and downward fluxes extend from each layer to each immediately underlying layer (much like local PBL schemes would). Much like the YSU scheme, the PBL height is determined by where the bulk Richardson number exceeds 0.25. The advantage of the ACM2 scheme is that it can depict the vertical profiles of potential temperatures and velocity in the PBL with greater accuracy than soley local or non-local schemes can (Pleim 2007a). Further validation of the ACM2 scheme has shown that it is able to support the PBL heights typically seen in afternoon wind profiler data and radar (Pleim 2007b). Like the YSU scheme, the ACM2 scheme also tends to overdeepen the PBL in deep convective environments (Coniglio et al. 2013). Very similar findings to these advantages and disadvantages were seen in Xie et al. (2012), where the choice of PBL schemes can result in sizable differences in the vertical profiles of temperature, moisture, and momentum in the boundary layer.

Li and Pu (2008) tested the sensitivity of the early rapid intensification of Hurricane Emily (2005) to microphysics and PBL parameterizations. The local (MYJ) and non-local (YSU) schemes tested showed a significant difference in intensity between these two schemes, producing a 19-hPa difference in simulated mean sea level pressure. The main reason for this difference was that the storms' internal structure, specifically the structure of the eyewall convective heating distribution, surface latent heat flux, and low-level equivalent potential temperature (θ_e), were strongly influenced by the PBL schemes. Nolan et al. (2009) evaluated PBL parameterizations in high-resolution simulations of Hurricane Isabel (2003). The local (MYJ) and the non-local (YSU) PBL schemes simulated tracks nearly identical to observations and were also able to reproduce a boundary layer with a shallow (∼600-m) well-mixed layer and a much deeper (∼1000-m) radial inflow layer (Nolan et al. 2009). Finally, in the examination of a tropical cyclone in the Bay of Bengal, a local (MYJ) PBL scheme produced higher ocean surface fluxes than the non-local (YSU) PBL scheme (Sateesh et al. 2017). The non-local (YSU) PBL scheme produced a better simulation with respect to winds and pressure distribution, cloud fraction, and track than the local (MYJ) PBL scheme. As stated before, it is likely that the local PBL scheme had difficulty transporting heat and moisture from the low levels to the upper levels.

The YSU, MYNN3, and ACM2 PBL schemes capture the variety of PBL parameterizations used operationally today in numerical weather prediction models. In this study, I will examine the sensitivities of tropical cyclone boundaries and rotating convection to these three PBL schemes. Some questions to answer include: How PBL parameterization affects the distribution, structure, and longevity of rotating and non-rotating convection in tropical cyclones, and do the PBL schemes alter how and where tropical cyclone boundaries form and how these boundaries change over time?

d. Tropical cyclone boundaries

Tropical cyclones do not have equal supercell potential everywhere as they tend to cluster near boundaries. There are two major types of boundaries that have been documented in observations of landfalling tropical cyclones. The first is areas of convergence of the low-level wind due to frictional differences between the ocean and land (Baker et al. 2009; Green et al. 2011). The second is baroclinic boundaries due to variations in temperature and moisture (Edwards and Pietrycha 2006). Convergent boundaries tend to enhance shear, while baroclinic boundaries can influence the distribution of CAPE. The warm and mid-level dry air side of baroclinic boundaries has increased CAPE. Edwards and Pietrycha (2006) suggests four distinct classes of boundaries and the relation to shear and CAPE that may influence tropical cyclone supercell and tornado potential.

The first is the buoyancy-limiting case, such that there is supportive vertical shear profiles on both sides, but sufficient CAPE only on one side of a boundary. The second is the shear-limiting case, such that there is supportive CAPE on both sides, but favorable shear on one side of the boundary. The third is the overlapping case, where there is supportive CAPE on one side and supportive vertical shear on the other side of a boundary. The last class is the null group, which would have no apparent organization of shear and CAPE. These four distinct classes of boundaries are likely to promote different risks as they relate to location of convection in tropical cyclones.

There is a stark difference in friction over the ocean and over land. This friction can have a large impact on the low-level winds in tropical cyclones. Powell and Houston (1998) suggested that changes in surface wind speed from ocean to land may be as large as 8–10 $\frac{m}{s}$ across horizontal distances of about 10 km. The winds around a tropical cyclone can be approximated as in gradient wind balance, which is a balance between the pressure gradient force (PGF), the centrifugal force ($\frac{mv^2}{r}$), and the Coriolis force ($2\Omega * v * sin(latitude)$). From gradient wind balance, drastic deceleration of the wind also has impacts on the wind direction. As the wind decelerates due to friction, it is deflected towards the center of the tropical cyclone as the centrifugal force is a function of the square of the velocity (v^2); thus, it becomes smaller faster than the Coriolis force which is only a function of velocity (v) while the PGF remains the same. In observations of Hurricane Ivan (2004), Baker et al. (2009) showed near surface wind speed changes from ocean to land of 2–4 $\frac{m}{s}$, which is not as large as what was proposed in Powell and Houston (1998). Baker et al. (2009) reported that it seemed plausible that rapidly moving supercells could experience drastically different low-level wind profiles within spans of a few kilometers in tropical cyclones during landfall. The change in wind speed and direction due to friction results in increased low-level shear (increased helicity), which climatological studies suggest is often associated with more frequent tornadoes (Markowski et al. 2003) and stronger mesocyclones (Baker et al. 2009)

The formation of baroclinic boundaries can happen through a variety of processes in the tropical cyclone envelope. Vescio et al. (1996) first noted that midlevel dry air intrusions have the potential to substantially alter the thermodynamic structure, which can influence tornado outbreaks and generate baroclinic boundaries in the tropical cyclone environment. Dry air intrusions into the tropical cyclone can result in local warming and, therefore, baroclinic boundaries (Edwards and Pietrycha 2006). Curtis (2004) found that tropical cyclones associated with tornado outbreaks exhibited three noteworthy environmental details. Tropical cyclones with tornado outbreaks had: lower LCLs, more moisture from the surface to 900 hPa, and, more dry air above 700 hPa, which is indicative of dry air intrusions, than the tropical cyclones that did not produce tornado outbreaks or the null cases. The lower LCL height is consistent with the both buoyancy-limiting case from Edwards and Pietrycha (2006) and the findings from Rasmussen and Blanchard (1998) who noted that the LCL height for soundings associated with tornadoes were significantly lower than for soundings associated with only supercells or even non-supercells across the United States. The resulting temperature and moisture differences caused by midlevel dry air intrusion creates baroclinic boundaries which can act as a catalyst for tornado outbreaks in tropical cyclones (Curtis 2004).

Baroclinic boundaries have been documented in both observations (Edwards and Pietrycha 2006) and in model simulations (Green et al. 2011; Card 2019) of tropical cyclones. Dry slots can lead to the formation of baroclinic boundaries due to differential surface heating within the tropical cyclone rainband region (Edwards and Pietrycha 2006). Relatively cloud-free areas between rainbands can support a few degrees Celsius of diabatic surface heating (Card 2019). The asymmetric surface warming can act to locally magnify CAPE and contribute to supercell maintenance (Edwards 2012).

Boundaries like those due to frictional differences between land and ocean surfaces and baroclinic gradients caused by gradients in temperature and/or moisture can help convection develop and mature near the coast during tropical cyclone landfall. Dry air intrusions can also act to increase convective instability invigorating convection and helping develop rotating convection in localized areas.

3. Questions and hypotheses

The purpose of this proposal is to investigate the role of microphysics and planetary boundary layer parameterizations on the structure, distribution, and development of rotating and non-rotating convection in tropical cyclones, as well as TC-scale boundaries

The first part of this study will investigate WSM6 and WDM6 microphysics parameterizations. The goal will be to determine the effects of microphysics parameterization on the distribution, structure, and longevity of convection in tropical cyclones. The second part will investigate local, non-local, and hybrid PBL parameterizations. As with microphysics, the goal is to determine the effects of PBL parameterizations on the distribution, structure, and longevity of convection in tropical cyclones. The third part will investigate boundaries at the tropical cyclone, or sub-tropical cyclone, scale and the impact on convection. The goal will be to understand how these boundaries form and affect the distribution of convection, and investigate how these boundaries change over time. The last part will focus on comparing local frictional effects that drive the weakening of the wind at the surface and compare those to the winds above the boundary layer to investigate if this can act to generate additional low-level helicity during tropical cyclone landfall.

Question 1: How does varying the microphysics and planetary boundary layer parameterizations affect tropical cyclone convection? Does this choice effect the distribution, structure, and longevity of rotating and non-rotating convection?

Hypothesis for question 1: Double and single moment microphysics parameterizations in warm rain processes have an effect on the development, structure, and longevity of tropical cyclone convection. The limited number of CCN in WDM6 is likely to limit spurious light precipitation. The limited CCN is also likely to reduce the amount of ice and graupel in the tropical cyclone. Reduction of graupel in the cloud would result in a more intense storm (McFarquhar et al. 2006; Fovell et al. 2009). The largest impact from the microphysics schemes will come from the diabatic heating and cooling, and the resulting consequences to the convective organization of the tropical cyclones.

Planetary boundary layer parameterizations act to vertically mix heat, moisture, and momentum, which affects the development and structure of tropical cyclone convection. The YSU scheme is likely to result in too much dry air at the surface near deep convective cells. It is expected that the MYNN3 PBL scheme will not fully account for the deep vertical mixing associated with large eddies in the tropical cyclone boundary layer, thus underestimating the vertical transport of heat, moisture, and momentum. This underestimate will likely result in less intense convection and result in less prominent tropical cyclone scale boundaries between the rainbands. ACM2 is non-local for upward fluxes and is likely to experience the same drawbacks as the YSU scheme, resulting in over deepening of the PBL. The ACM2 PBL scheme is likely to simulate realistic vertical temperature and wind profiles due to the combination of local and non-local fluxes. For these reasons, the choice of microphysics and PBL parameterization is likely to affect the distribution, structure, and longevity of rotating and non-rotating convection.

Question 2: Are there boundaries at the tropical cyclone, or sub-tropical cyclone, scale that help develop or intensify convection locally? Is there a link between dry air intrusion and the development baroclinic boundaries, and does this affect rotating convection? How do baroclinically- and convergence-forced boundaries change over time? How do the choice of microphysics and PBL parameterization affect these boundaries?

Hypothesis for question 2: Boundaries, like those due to frictional differences between land and ocean surfaces and baroclinic gradients, helps convection develop and mature near the coast during tropical cyclone landfall. Dry air intrusions act to increase convective instability invigorating convection locally near these boundaries. Dry air intrusion can also result in clearing between rainbands leading to the development of surface baroclinic boundaries due to enhanced insolation, as seen in Card (2019). Both convergent and baroclinic boundaries help develop and enhance upward vertical motion in localized areas, causing clustering of convection. Microphysics parameterizations, particularly the lack of spurious reflectivity (i.e., clearing) will result in stronger and more frequent baroclinic boundaries with the WDM6 microphysics scheme. PBL parameterizations can also affect boundaries in tropical cyclones since they govern the vertical transport of momentum, moisture, and temperature. The local PBL scheme (MYNN3) will have difficulty transporting heat and moisture fluxes from the surface to the layers above. The low-level distribution of heat and moisture will affect the formation, and intensity, of baroclinic boundaries and CAPE. Momentum differences between the PBL schemes will result in less vertical shear in the schemes that do not propagate the effects of surface friction aloft.

Question 3: Does the rate of weakening at the surface (due to frictional effects), compared to above the boundary layer, generate additional low-level helicity in localized areas during landfall?

Hypothesis for question 3: Friction at the surface during landfall will act to weaken near surface winds faster than winds aloft, generating additional low-level helicity in localized regions over land. This increased low-level helicity (0–3-km) can greatly increase the likelihood of tornadogenesis at landfall from an increase in mesocyclone strength. Prior studies have suggested that development of tropical cyclone supercells is linked to the increase in friction as cells transition from the ocean to land, acting to increase low-level helicity (Gentry 1983; Baker et al. 2009). Edwards (2012) noted that as tropical cyclones move inland, the wind profiles do not weaken uniformly, which can generate additional low-level helicity. This phenomenon was shown in both hurricanes Beryl (1994) and Ivan (2004). Weakening at the surface due to friction will locally increase vertical wind shear over land, generating stronger mesocyclones as rotating convection makes landfall in the tropical cyclone.

4. Methodology

a. Model setup

For this research, the Advanced Research WRF version 4.1 will be used in both the static and vortex following nest configurations. To efficiently use computing resources, an adaptive time step will also be utilized in all simulations. Each storm will be simulated in two separate steps, a 9-km run and then a separate 3-km run with a 1-km vortex following nest.

First, a 9-km horizontal grid spacing simulation (Domain 1) will be used to provide the initial and boundary conditions to the higher-resolution, and vortex-following, nests in the second set of simulations [Figs. 6a (350 X 300 gridpoints) and 7a (300 X 350 gridpoints)]. Domain 1 is run from 0000 UTC 24 August through 1200 UTC 27 August for Hurricane Harvey (2017) and 1200 UTC 8 September through 0000 UTC 12 September for Hurricane Irma (2017). These times allow 24h for the model to spin up prior to using it as initial and boundary conditions for the second set of simulations. The ERA5 (Copernicus Climate Change Service (C3S) 2019) is used for the initial and boundary conditions for the 9-km domain at three-hourly intervals. To help the simulation develop the storms' intensity and convection faster, the cumulus parameterization scheme New Tiedtke (Zhang and Wang 2017) was used. For consistency, the 9-km domain is run in multiple configurations covering all the combinations of microphysics and PBL parameterizations to be tested in the second set of simulations. All of the 9-km simulations have a 10-hPa model top with 50 vertical levels.

The 3-km static domain (Domain 2) in the second set of simulations will use the 9-km simulation as initial and boundary conditions [Figs. 6b (750 X 600 gridpoints) and 7b (600 X 750 gridpoints)]. The 1-km vortex following domain (Domain 3) is nested within Domain 2 [Figs. 6b and 7b (901 X 901 gridpoints)]. Convective processes will be explicitly resolved in the 3-km and 1-km domains, therefore no convective parameterization will be used. Both Domain 2 and 3 will have a 50-hPa model top with 50 vertical levels. In each of these simulations, the microphysics and PBL schemes will be the only parameterizations varied. Domains 2 and 3 will be run from 0000 UTC 25 August through 1200 UTC 27 August for Hurricane Harvey (2017) and 1200 UTC 9 September through 0000 UTC 12 September for Hurricane Irma (2017). This timing will provide a 12-h adjustment period from model start to the analysis times.

The WRF model configuration will be set following previous tropical cyclone studies (e.g., Gentry and Lackmann 2010; Sun and Barros 2012, 2014; Lackmann 2015; Carroll-Smith 2018). All three domains for each simulation will use: the updated Rapid Radiative Transfer Model

(RRTMG; Iacono et al. 2008) longwave and shortwave radiation schemes; the revised National Center for Atmospheric Research (NCAR) fifth-generation Mesoscale Model (MM5) Monin-Obukhov (Jiménez et al. 2012) surface layer parameterization; and, the Noah land surface model (Chen and Dudhia 2001). To improve the tropical cyclone surface fluxes the "isftcflx" option is activated such that Donelan and Garratt formulations are used to calculate the surface moist enthalpy and momentum exchange coefficients in the surface layer (Lackmann 2015). Individual model parameterizations for each domain are located in Table 1.

b. Model track and intensity verification

Figure 8a shows that the track of Hurricane Harvey (2017) in the 9-km simulation was very similar to the observed track in the Atlantic Best Track (Landsea and Franklin 2013) from 0000 UTC 24 August through 1200 UTC 27 August. Early in the 9-km simulation, the track of Harvey is slightly too far south between 0600 UTC 24 August through 0000 UTC 25 August. As a result, the 1-km simulations, shown in Figure 8b, are initialized slightly too far south and continue on a track south of that observed in the Best Track. The 1-km simulations penetrated further inland before beginning to turn back out to sea.

Figure 9a shows that the 9-km WRF simulation of Hurricane Harvey was initialized at a similar intensity to the observed Harvey, but remained much weaker than observed in the Atlantic Best Track from 0300 UTC 24 August through 1200 UTC 26 August. There is a divergence of the model simulations at 0000 UTC 25 August where the model simulations using the MYNN3 PBL scheme do not strengthen as rapidly as the other simulations. The most intense run is the model simulation using WDM6 microphysics and YSU PBL parameterizations, reaching a minimum sea level pressure of 965 hPa compared to the observed minimum sea level pressure of 942 hPa. Figure 9b shows that the 1-km WRF simulations were initialized at a weaker intensity than what was observed in the Best Track. The 1-km simulation using the MYNN3 PBL scheme also showed a weaker intensity compared to the other simulations over the first 24 h of the simulation.

Figure 10a shows that the track of Hurricane Irma (2017) in the 9-km simulation was very similar to the observed track in the Atlantic Best Track from 1200 UTC 8 September through 0000 UTC 12 September. Like the 9-km simulations, the 1-km simulations, shown in Figure 10b, produce very similar tracks to the Best Track along the entire analysis time.

Figure 11a shows that the 9-km WRF simulation of Hurricane Irma was initialized and remained much weaker than the observed intensity from the Atlantic Best Track. This discrepancy in the intensity is not surprising since coarse resolution models such as the ERA5 (0.25° X 0.25°), which was used to initialize the 9-km WRF, had a minimum sea level pressure at 1200 UTC 8 September of about 960 hPa. Though the simulations of Hurricane Harvey did better with respects to intensity than the Hurricane Irma simulation, this is most likely due to the fact that Hurricane Harvey was much weaker in observations at the start of the simulation compared to Hurricane Irma. The 9-km WRF simulations have Hurricane Irma maintaining intensity between 955 and 970 hPa before beginning to weaken after 0000 UTC 11 September. It is seen again that the two weakest runs were the simulations using the MYNN3 PBL scheme. Figure 11b shows that the 1-km simulations of Hurricane Irma were stronger than the 9-km simulations; however, the 1-km simulation did not become as intense as the observations from the Best Track. Like the 9-km simulation, the WDM6–MYNN3 1-km simulation produced a less intense storm.

Although the simulations of both hurricanes Harvey and Irma (2017) are weaker than the observed storms and took slightly different tracks, the simulations show similar tracks and intensities to each other. These similarities will allow for a clean comparison between the differences produced by changing the microphysics and boundary layer parameterizations.

c. Diagnostics

A series of analyses will be used to investigate the interactions between microphysics and planetary boundary layer parameterizations on the development and structure of tropical cyclone convection. The first analysis will focus on the distribution and structure of rotating and non-rotating convection. The second analysis will focus on the location and evolution of frictional and baroclinic boundaries in the tropical cyclones, and how these boundaries vary with different microphysics and planetary boundary layer schemes. A mesoscale analysis will be used to investigate the interactions between various types of boundaries and convection in the rainbands of tropical cyclones. This study is unique in that it plans to investigate the interactions between microphysics and planetary boundary layer parameterizations on the development, evolution, and structure of both tropical cyclone convection and boundaries during landfall.

1) Distribution and structure of rotating and non-rotating convection

To investigate the interaction between microphysics and PBL parameterizations on the distribution of rotating and non-rotating convection, an analysis similar to the techniques of Card (2019) and Carroll-Smith et al. (2019) will be done on the 1-km WRF domain. First, individual convective cells will be identified using local maxima in model reflectivity exceeding the 99.9^{th} percentile across all the hours of a simulation. The identified cells will be referred to as rotating convective cells if the 0–3-km updraft helicity exceeds the 99.95^{th} similar to Carroll-Smith et al. (2019). The identified cells that had values of 0–3-km updraft helicity less than or equal to zero and that did exceed the 99.9^{th} percentile in updraft velocity, will be referred to as non-rotating convective cells. Based on these criteria, the non-rotating convective cells have no updraft helicity but strong updraft velocities, while rotating cells have large updraft helicity. These percentile values for hurricanes Harvey and Irma (2017) can be seen in Tables 2 and 3, respectively.

In these thresholds is where we see the first indication of differences across microphysics and PBL schemes. The 99.9^{th} percentile in model reflectivity, 99.9^{th} percentile in updraft velocity, and the 99.95^{th} percentile in 0–3-km updraft helicity were all statistically significantly[1] different across the micorphsycis and PBL parameterizations. In Tables 2 and 3, the 99.9^{th} percentile in model reflectivity is statistically significantly lower in the simulations using the WDM6 microphysics scheme compared to WSM6 simulations using the same PBL scheme. This result was expected as past research has shown that WDM6 tends to produce less spurious reflectivity than WSM6 (Hong et al. 2010). Tables 2 and 3 also show that the 99.9^{th} percentile in updraft velocity and the 99.95^{th} percentile in 0–3-km updraft helicity was statistically significantly lower in the simulations using the MYNN3 PBL scheme.

After identification, the rotating and non-rotating convection distributions across the two microphysics and three PBL parameterizations will be examined. The distributions will be examined with respect to vertical wind shear and with respect to geographic north. Card (2019) and the storm tracks in Figures 8 and 10 showed that for hurricanes Harvey and Irma (2017), the storm motion was mostly northerly making the results very comparable to the distributions with respect to geographic north. In Card (2019), the number of identified rotating storms outnumbered the identified non-rotating storms by a factor of 2–3 in both Harvey and Irma (2017). In Hurricane Harvey, most rotating and non-rotating storms occurred directly downshear, with non-rotating storms generally occurring at more distant radii (Fig. 4). Most of the rotating storms in Hurricane Irma occurred directly downshear, while most of the non-rotating storms occurred upshear right in both the NCAR ensemble and in observations (Fig. 5). Once cell types are identified, how varying the microphysics and planetary boundary layer schemes changes the spatial distribution of rotating and non-rotating convective cells will be examined.

[1]Statistical significance is determined via a two sided t-test for the means of two independent samples at the 99% confidence level.

Finally, vertical cross sections will be done through a few of the select rotating and non-rotating cells to examine the vertical structure and spatial distributions of mixing ratios of water vapor, rain, and ice across the different microphysics parameterizations. Vertical cross sections will also be done for select rotating and non-rotating convective cells to examine the vertical structure and boundary layer interactions in the lowest 3 km. Similarly to Didlake and Houze (2009), who did cross sections of Hurricane Katrina (2005) during the Rainband and Intensity Change Experiment (RAINEX), these cross sections will be used to investigate how convective scale wind flow and other convective scale features within the individual cells.

The goals of the investigation into the distribution, structure, and longevity of rotating and non-rotating convection are to investigate Question one.

2) Frictional and baroclinic boundaries

Boundaries, both induced by friction and those induced by baroclinic features will be investigated along the Texas coast in Hurricane Harvey and the Florida coast in Hurricane Irma in the 1-km simulations. Boundaries induced by friction will be identified by diagnosing the wind field near the coastline, while baroclinic boundaries will be identified using gradients in temperature, relative humidity, and MUCAPE (most unstable CAPE). Furthermore, vertical cross sections of these boundaries will help in understanding the depth of these features, how they may change or move over time, and how they affect convection. In association with Question one, differences in the boundaries based on the microphysics and PBL parameterizations will be examined.

An analysis of the three-dimensional frontogenesis equation (eq. 1) will provide insight into which terms might be important in tropical cyclone boundary formation:

$$
\begin{aligned}
F = \frac{1}{|\nabla\theta|}\Bigg[&\frac{\partial\theta}{\partial x}\left\{\frac{1}{C_p}\left(\frac{p_\circ}{p}\right)^{\kappa}\left[\frac{\partial}{\partial x}\left(\frac{dQ}{dt}\right)\right]-\left(\frac{\partial u}{\partial x}\frac{\partial\theta}{\partial x}\right)-\left(\frac{\partial v}{\partial x}\frac{\partial\theta}{\partial y}\right)-\left(\frac{\partial w}{\partial x}\frac{\partial\theta}{\partial z}\right)\right\}\\
&+\frac{\partial\theta}{\partial y}\left\{\frac{1}{C_p}\left(\frac{p_\circ}{p}\right)^{\kappa}\left[\frac{\partial}{\partial y}\left(\frac{dQ}{dt}\right)\right]-\left(\frac{\partial u}{\partial y}\frac{\partial\theta}{\partial x}\right)-\left(\frac{\partial v}{\partial y}\frac{\partial\theta}{\partial y}\right)-\left(\frac{\partial w}{\partial y}\frac{\partial\theta}{\partial z}\right)\right\}\\
&+\frac{\partial\theta}{\partial z}\left\{\frac{p_\circ^{\kappa}}{C_p}\left[\frac{\partial}{\partial z}\left(p^{-\kappa}\frac{dQ}{dt}\right)\right]-\left(\frac{\partial u}{\partial z}\frac{\partial\theta}{\partial x}\right)-\left(\frac{\partial v}{\partial z}\frac{\partial\theta}{\partial y}\right)-\left(\frac{\partial w}{\partial z}\frac{\partial\theta}{\partial z}\right)\right\}\Bigg]
\end{aligned}
\tag{1}
$$

where theta (θ) is the potential temperature, C_p is the specific heat at constant pressure ($1006\frac{J}{kgK}$), p is the pressure, $p_\circ$ is a reference pressure (1000hPa), κ is a constant [$\frac{R}{C_p}$, 0.286], Q is diabatic heating, u is the zonal wind, and v is the meridional wind. The three-dimensional frontogenesis equation can be broken up into four major components; 1) the diabatic terms (eq. 2), 2) the deformation terms (eq. 3), 3) the tilting terms (eq. 4), and 4) the vertical divergence term (eq. 5). The tilting term (eq. 4) can not generate gradients in potential temperature, it can only transform vertical gradients into the horizontal and, therefore, will not be included in the analysis of the three-dimensional frontogenesis equation.

$$
Diabatic = \frac{1}{C_p}\left(\frac{p_\circ}{p}\right)^{\kappa}\left[\frac{\partial}{\partial x}\left(\frac{dQ}{dt}\right)\right]+\frac{1}{C_p}\left(\frac{p_\circ}{p}\right)^{\kappa}\left[\frac{\partial}{\partial y}\left(\frac{dQ}{dt}\right)\right]+\frac{p_\circ^{\kappa}}{C_p}\left[\frac{\partial}{\partial z}\left(p^{-\kappa}\frac{dQ}{dt}\right)\right] \tag{2}
$$

$$
\begin{aligned}
Deformation = &-\left(\frac{\partial u}{\partial x}\frac{\partial\theta}{\partial x}\right)-\left(\frac{\partial v}{\partial x}\frac{\partial\theta}{\partial y}\right)\\
&-\left(\frac{\partial u}{\partial y}\frac{\partial\theta}{\partial x}\right)-\left(\frac{\partial v}{\partial y}\frac{\partial\theta}{\partial y}\right)\\
&-\left(\frac{\partial u}{\partial z}\frac{\partial\theta}{\partial x}\right)-\left(\frac{\partial v}{\partial z}\frac{\partial\theta}{\partial y}\right)
\end{aligned}
\tag{3}
$$

$$
Tilting = -\left(\frac{\partial w}{\partial x}\frac{\partial\theta}{\partial z}\right)-\left(\frac{\partial w}{\partial y}\frac{\partial\theta}{\partial z}\right) \tag{4}
$$

$$
Vertical\,Divergence = -\left(\frac{\partial w}{\partial z}\frac{\partial\theta}{\partial z}\right) \tag{5}
$$

To determine the diabatic heating rate ($\frac{dQ}{dt}$) needed for the diabatic term in the three-dimensional kinematic frontogenesis equation (eq. 2), I will use the temperature tendency equation (eq. 6) after applying the first law of thermodynamics (eq. 7) as in Yanai et al. (1973).

$$\frac{dT}{dt} = \frac{\partial T}{\partial t} + \vec{V} \cdot \nabla T \tag{6}$$

$$\frac{dT}{dt} = -\frac{g}{c_p} w + \frac{1}{c_p} \frac{dQ}{dt} \tag{7}$$

Combining equations 6 and 7 and reorganizing produces an equation for the diabatic heating rate (eq. 8).

$$\frac{dQ}{dt} = c_p \left(\frac{\partial T}{\partial t} + \vec{V} \cdot \nabla T + \frac{g}{c_p} w \right) \tag{8}$$

This study will look at the diabatic (eq. 2), deformation (eq. 3), and vertical divergence (eq. 5) terms and preform a scale analysis to determine which terms may play the largest role in the tropical cyclone environment. The overarching goals of the investigation into the frictional and baroclinic boundaries during landfall are to address Questions two and three.

5. Preliminary findings

a. Cell distribution thresholds

Preliminary results from the cell distribution thresholds has provided some interesting results. As seen from the 99.95^{th} percentile values of the 0–3-km updraft helicity in Tables 2 and 3, the MYNN3 PBL scheme produces statistically significantly lower values than either the YSU or ACM2 schemes. There are two terms which contribute to 0–3-km updraft helicity, the vertical velocity and the 0–3-km helicity. To understand the differences in these two terms we will focus on 1800 UTC 26 August for Hurricane Harvey and 1800 UTC 10 September for Hurricane Irma. Figures 12 and 13 show the differences in maximum updraft velocity between the MYNN3 PBL scheme and the other two PBL schemes. The differences are mainly on the convective scale, showing where there is convection in each simulation there is strong vertical motion. In both hurricanes Harvey and Irma, large differences in convection are located on the eastern half of the storms. The location of the convection is not highly spatially correlated between the simulations.

Figures 14 and 15 show the differences in 0–3-km helicity between the MYNN3 PBL scheme and the other two PBL schemes at these times. These differences are larger in spatial scale than those of the vertical velocities. The differences in the 0–3-km helicity are mainly on the northern side of the storm in both hurricanes Harvey and Irma, which happens to be the land side of the storm.

The planetary boundary layer height can be used to understand how the simulations are interacting with the land and how deep the vertical mixing is in this area of the storm. This will provide incite as to why the spatial pattern of 0–3-km helicity may be different over land. Figure 16 shows the PBL heights for the simulations. For both storms the PBL heights tend to be much deeper over land in the YSU and ACM2 PBL schemes, compared to the MYNN3 scheme. Future work will included diagnosing how the depth of the PBL between theses simulations affects the low-level helicity, and continuing to explore the questions posed in Question one.

b. Boundaries

Preliminary results from the frontogenesis equation for Hurricane Harvey at 1800 UTC 26 August and Hurricane Irma at 1800 UTC 10 September are shown in Figure 17. For the simulations using WSM6–YSU parameterizations, both storms show that the diabatic heating term is the leading term in the full frontogenesis equation. Figure 18 shows the outgoing longwave radiation as a proxy for convection intensity, where colder cloud tops signify more vigorous convection. Theses differences in convection are highlighted in the diabatic heating term of the frontogenesis equation in Figure 17. In the WSM6–YSU and WDM6–YSU simulations, the coldest cloud tops are located to the northeast of the center of both hurricanes Harvey and Irma (Fig. 18). In WDM6–YSU simulation for Hurricane Irma (Fig. 18d), warm cloud tops can be seen surrounding the center of the storm, unlike in the WSM6–YSU simulation (Fig. 18b).

The deformation terms in the frontogenesis equation are strongly tied to horizontal gradients in potential temperature gradients (Fig. 17). In both hurricanes Harvey and Irma, areas with lower relative humidity display potential temperatures of about 2 K warmer compared to the moist areas (Fig. 19), which is very similar to what was seen in Card (2019). There tends to be a larger areal spread of high relative humidity in the WDM6–YSU simulations if both hurricanes Harvey and Irma (Fig. 19c and 19d).

These preliminary results suggest that in both the simulations of hurricanes Harvey and Irma that prescribed PBL and microphysics parameterizations will impact frontogenesis. Both the diabatic heating from differences in convection in the tropical cyclone and the deformation of temperature gradients in relation to areas of lower relative humidity and wind. Future work will focus on continuing to explore the questions posed in Questions two and three.

6. Timeline of Work

Summer 2020:

- Begin writing introduction, literature review, and methods sections of the dissertation
- Continue analysis for all hypothesis

Fall 2020:

- Begin writing results chapters
- Edit full Ph.D. dissertation

December 2020:

- Defend Ph.D. dissertation.

Acknowledgments. I would like to thank all of my committee members for their help and support as I continue to become a better scientist. I want to provide a special thank you to my advisor, Dr. Kristen Corbosiero for all of her support and encouragement. I have had support from many of the graduate students in this department including but not limited to the various members of TC Dynasty over the past few years and my office colleagues in ES 330. I'd also like to thank Kevin Tyle for assistance with local computing and storage, as well as the entire DAES faculty and staff for their assistance. I would also like to acknowledge high-performance computing support from Cheyenne (doi:10.5065/D6RX99HX) provided by NCAR's Computational and Information Systems Laboratory, sponsored by the National Science Foundation (Computational and Information Systems Laboratory 2019).

References

Bai, L., Z. Meng, K. Sueki, G. Chen, and R. Zhou, 2019: Climatology of tropical cyclone tornadoes in china from 2006 to 2018. *Sci. China Earth Sci.*, **63**, 1–15.

Baker, A. K., M. D. Parker, and M. D. Eastin, 2009: Environmental ingredients for supercells and tornadoes within Hurricane Ivan. *Wea. Forecasting*, **24**, 223–224.

Brotzge, J., S. Erickson, and H. Brooks, 2011: A 5-yr climatology of tornado false alarms. *Wea. Forecasting*, **26**, 534–544.

Card, D., 2019: A multiscale analysis of the rainband and cellular structure in hurricanes Harvey and Irma (2017) using the NCAR Ensemble. M.S. thesis, Department of Atmospheric and Environmental Science, University at Albany, 127 pp., URL https://search.proquest.com/docview/2318188203?accountid=14166.

Carroll-Smith, D. L., 2018: "If it happened in..." a pseudo-global warming assessment of tropical cyclone tornadoes. Ph.D. thesis, University of Illinois at Urbana-Champaign, URL https://www.ideals.illinois.edu/handle/2142/101477.

Carroll-Smith, D. L., L. C. Dawson, and R. J. Trapp, 2019: High-resolution real-data WRF modeling and verification of tropical cyclone tornadoes associated with Hurricane Ivan (2004). *Electronic J. Severe Storms Meteor.*, **14**, 1–36.

Chen, F., and J. Dudhia, 2001: Coupling an advanced land surface– hydrology model with the Penn State–NCAR MM5 modeling system. Part I: Model description and implementation. *Mon. Wea. Rev.*, **129**, 569–585.

Cohard, J.-M., and J.-P. Pinty, 2000: A comprehensive two-moment warm microphysical bulk scheme. i: Description and tests. *Quart. J. Roy. Meteor. Soc.*, **126**, 1815–1842.

Computational and Information Systems Laboratory, 2019: Cheyenne: HPE/SGI ICE XA System (University Community Computing). National Center for Atmospheric Research, Boulder, CO, doi:10.5065/D6RX99HX.

Coniglio, M. C., J. Correia Jr, P. T. Marsh, and F. Kong, 2013: Verification of convection-allowing wrf model forecasts of the planetary boundary layer using sounding observations. *Wea. Forecasting*, **28**, 842–862.

Copernicus Climate Change Service (C3S), 2019: ERA5: Fifth generation of ecmwf atmospheric reanalyses of the global climate. Copernicus Climate Change Service Climate Data Store (CDS), URL https://cds.climate.copernicus.eu/cdsapp#!/home.

Corbosiero, K. L., and J. Molinari, 2003: The relationship between storm motion, vertical wind shear, and convective asymmetries in tropical cyclones. *J. Atmos. Sci.*, **60**, 366–376.

Curtis, L., 2004: Midlevel dry intrusions as a factor in tornado outbreaks associated with landfalling tropical cyclones from the Atlantic and Gulf of Mexico. *Wea. Forecasting*, **19**, 411–427.

Didlake, A. C., and R. A. Houze, 2009: Convective-scale downdrafts in the principal rainband of Hurricane Katrina (2005). *Mon. Wea. Rev.*, **137**, 3269–3293.

Eastin, M. D., and M. C. Link, 2009: Miniature supercells in an offshore outer rainband of Hurricane Ivan (2004). *Mon. Wea. Rev.*, **137**, 2081–2104.

Edwards, R., 2010: Tropical cyclone tornado records for the modernized national weather service era. *Preprints, 25th Conf. on Severe Local Storms, Denver, CO, Amer. Meteor. Soc. P*, Vol. 2.

Edwards, R., 2012: Tropical cyclone tornadoes: A review of knowledge in research and prediction. *Electronic J. Severe Storms Meteor.*, **7**, 1–61.

Edwards, R., and A. E. Pietrycha, 2006: Archetypes for surface baroclinic boundaries influencing tropical cyclone tornado occurrence. *AMS 23nd Conf. Severe Local Storms*, St. Louis MO, Storm Prediction Center, URL https://www.spc.ncep.noaa.gov/publications/edwards/tcfronts.pdf.

Fovell, R. G., Y. P. Bu, K. L. Corbosiero, W.-w. Tung, Y. Cao, H.-C. Kuo, L.-h. Hsu, and H. Su, 2016: Influence of cloud microphysics and radiation on tropical cyclone structure and motion. *Meteorol. Monogr.*, **56**, 1–26.

Fovell, R. G., K. L. Corbosiero, and H.-C. Kuo, 2009: Cloud microphysics impact on hurricane track as revealed in idealized experiments. *J. Atmos. Sci.*, **66**, 1764–1778.

Fovell, R. G., K. L. Corbosiero, A. Seifert, and K.-N. Liou, 2010: Impact of cloud-radiative processes on hurricane track. *Geophys. Res. Lett.*, **37**.

Fovell, R. G., and H. Su, 2007: Impact of cloud microphysics on hurricane track forecasts. *Geophys. Res. Lett.*, **34**.

Gentry, M. S., and G. M. Lackmann, 2010: Sensitivity of simulated tropical cyclone structure and intensity to horizontal resolution. *Mon. Wea. Rev.*, **138**, 688–704.

Gentry, R. C., 1983: Genesis of tornadoes associated with hurricanes. *Mon. Wea. Rev.*, **111**, 1793–1805.

Green, B. W., F. Zhang, and P. Markowski, 2011: Multiscale processes leading to supercells in the landfalling outer rainbands of Hurricane Katrina (2005). *Wea. Forecasting*, **26**, 828–847.

Hong, S.-Y., and J.-O. J. Lim, 2006: The WRF single-moment 6-class microphysics scheme (wsm6). *J. Kor. Meteor. Soc.*, **42**, 129–151.

Hong, S.-Y., K.-S. S. Lim, Y.-H. Lee, J.-C. Ha, H.-W. Kim, S.-J. Ham, and J. Dudhia, 2010: Evaluation of the wrf double-moment 6-class microphysics scheme for precipitating convection. *Adv. Meteorol.*, **2010**, 707 253.

Hong, S.-Y., Y. Noh, and J. Dudhia, 2006: A new vertical diffusion package with an explicit treatment of entrainment processes. *Mon. Wea. Rev.*, **134**, 2318–2341.

Houze, R. A., 2010: Clouds in tropical cyclones. *Mon. Wea. Rev.*, **138**, 293–344.

Iacono, M. J., J. S. Delamere, E. J. Mlawer, M. W. Shephard, S. A. Clough, and W. D. Collins, 2008: Radiative forcing by long-lived greenhouse gases: Calculations with the aer radiative transfer models. *Geophys. Res. Lett.*, **113**, D13 103.

Jiménez, P. A., J. Dudhia, J. F. González-Rouco, J. Navarro, J. P. Montávez, and E. García-Bustamante, 2012: A revised scheme for the WRF surface layer formulation. *Mon. Wea. Rev.*, **140**, 898–918.

Kepert, J. D., 2012: Choosing a boundary layer parameterization for tropical cyclone modeling. *Mon. Wea. Rev.*, **140**, 1427–1445.

Lackmann, G. M., 2015: Hurricane sandy before 1900 and after 2100. *Bull. Amer. Meteor. Soc.*, **96**, 547–560.

Landsea, C. W., and J. L. Franklin, 2013: Atlantic hurricane database uncertainty and presentation of a new database format. *Mon. Wea. Rev.*, **141**, 3576–3592.

Li, X., and Z. Pu, 2008: Sensitivity of numerical simulation of early rapid intensification of Hurricane Emily (2005) to cloud microphysical and planetary boundary layer parameterizations. *Mon. Wea. Rev.*, **136**, 4819–4838.

Lim, K.-S. S., and S.-Y. Hong, 2010: Development of an effective double-moment cloud microphysics scheme with prognostic cloud condensation nuclei (CCN) for weather and climate models. *Mon. Wea. Rev.*, **138**, 1587–1612.

Lord, S. J., and J. M. Lord, 1988: Vertical velocity structures in an axisymmetric, nonhydrostatic tropical cyclone model. *J. Atmos. Sci.*, **45**, 1453–1461.

Markowski, P., C. Hannon, J. Frame, E. Lancaster, A. Pietrycha, R. Edwards, and R. L. Thompson, 2003: Characteristics of vertical wind profiles near supercells obtained from the rapid update cycle. *Wea. Forecasting*, **18**, 1262–1272.

Martinaitis, S. M., 2017: Radar observations of tornado-warned convection associated with tropical cyclones over Florida. *Wea. Forecasting*, **32**, 165–186.

McCaul, E., 1987: Observations of the Hurricane Danny tornado outbreak of 16 August 1985. *Mon. Wea. Rev.*, **115**, 1206–1223.

McCaul, E., 1991: Buoyancy and shear characteristics of hurricane tornado. *Mon. Wea. Rev.*, **119**, 1954–1978.

McCaul, E., and M. Weisman, 1996: Simulations of shallow supercell storms in landfalling hurricane environments. *Mon. Wea. Rev.*, **124**, 408–429.

McCaul, E. W., and M. L. Weisman, 2001: The sensitivity of simulated supercell structure and intensity to variations in the shapes of environmental buoyancy and shear profiles. *Mon. Wea. Rev.*, **129**, 664–687.

McFarquhar, G. M., H. Zhang, G. Heymsfield, J. B. Halverson, R. Hood, J. Dudhia, and F. Marks Jr, 2006: Factors affecting the evolution of hurricane erin (2001) and the distributions of hydrometeors: Role of microphysical processes. *J. Atmos. Sci.*, **63**, 127–150.

Molinari, J., and D. Vollaro, 2010: Distribution of helicity, CAPE, and shear in tropical cyclones. *J. Atmos. Sci.*, **67**, 274–284.

Nakanishi, M., and H. Niino, 2006: An improved Mellor–Yamada level-3 model: Its numerical stability and application to a regional prediction of advection fog. *Bound.-Lay. Meteorol.*, **119**, 397–407.

Nakanishi, M., and H. Niino, 2009: Development of an improved turbulence closure model for the atmospheric boundary layer. *J. Meteor. Soc. of Japan. Ser. II*, **87**, 895–912.

Nolan, D. S., J. A. Zhang, and D. P. Stern, 2009: Evaluation of planetary boundary layer parameterizations in tropical cyclones by comparison of in situ observations and high-resolution simulations of hurricane isabel (2003). part i: Initialization, maximum winds, and the outer-core boundary layer. *Mon. Wea. Rev.*, **137**, 3651–3674.

Novlan, D., and W. Gray, 1974: Hurricane-spawned tornadoes. *Mon. Wea. Rev.*, **102**, 476–488.

NWS, 2012: Hurricane Irene, August 21-30, 2011. Tech. rep., NOAA/NWS Service Assessment, 129 pp. URL https://www.weather.gov/media/publications/assessments/Irene2012.pdf.

Pleim, J. E., 2007a: A combined local and nonlocal closure model for the atmospheric boundary layer. part i: Model description and testing. *J. Appl. Meteor. Climatol.*, **46**, 1383–1395.

Pleim, J. E., 2007b: A combined local and nonlocal closure model for the atmospheric boundary layer. part ii: Application and evaluation in a mesoscale meteorological model. *J. Appl. Meteor. Climatol.*, **46**, 1396–1409.

Powell, M. D., and S. H. Houston, 1998: Surface wind fields of 1995 hurricanes erin, opal, luis, marilyn, and roxanne at landfall. *Mon. Wea. Rev.*, **126**, 1259–1273.

Putnam, B. J., M. Xue, Y. Jung, G. Zhang, and F. Kong, 2017: Simulation of polarimetric radar variables from 2013 caps spring experiment storm-scale ensemble forecasts and evaluation of microphysics schemes. *Mon. Wea. Rev.*, **145**, 49–73.

Rasmussen, E. N., and D. O. Blanchard, 1998: A baseline climatology of sounding-derived supercell andtornado forecast parameters. *Wea. Forecasting*, **13**, 1148–1164.

Sateesh, M., C. Srinivas, and P. Raju, 2017: Numerical simulation of tropical cyclone thane: role of boundary layer and surface drag parameterization schemes. *Nat. Hazards*, **89**, 1255–1271.

Schultz, L. A., and D. J. Cecil, 2009: Tropical cyclone tornadoes, 1950–2007. *Mon. Wea. Rev.*, **137**, 3471–3484.

Sun, X., and A. P. Barros, 2012: The impact of forcing datasets on the high-resolution simulation of Tropical Storm Ivan (2004) in the Southern Appalachians. *Mon. Wea. Rev.*, **140**, 3300–3326.

Sun, X., and A. P. Barros, 2014: High resolution simulation of Tropical Storm Ivan (2004) in the Southern Appalachians: role of planetary boundary-layer schemes and cumulus parametrization. *Quart. J. Roy. Meteor. Soc.*, **140**, 1847–1865.

Tao, W.-K., J. J. Shi, S. S. Chen, S. Lang, P.-L. Lin, S.-Y. Hong, C. Peters-Lidard, and A. Hou, 2011: The impact of microphysical schemes on hurricane intensity and track. *Asia-Pacific J. Atmos. Sci.*, **47**, 1–16.

Verbout, S. M., D. M. Schultz, L. M. Leslie, H. E. Brooks, D. J. Karoly, and K. L. Elmore, 2007: Tornado outbreaks associated with landfalling hurricanes in the North Atlantic Basin: 1954–2004. *Meteor. Atmos. Phys.*, **97**, 255–271.

Vescio, M. D., S. J. Weiss, and F. P. Ostby, 1996: Tornadoes associated with Tropical Storm Beryl. *Natl. Wea. Dig.*, **21**, 2–10.

Weiss, S., 1987: Some climatological aspects of forecasting tornadoes associated with tropical cyclones. *Preprints, 17th Conf. on Hurricanes and Tropical Meteorology*, Amer. Meteor. Soc., Miami, FL, 160–163.

Willoughby, H. E., F. D. Marks, and R. J. Feinberg, 1984: Stationary and moving convective bands in hurricanes. *J. Atmos. Sci.*, **41**, 3189–3211.

Xie, B., J. C. Fung, A. Chan, and A. Lau, 2012: Evaluation of nonlocal and local planetary boundary layer schemes in the WRF model. *J. Geophys. Res.*, **117**, D12 103.

Yanai, M., S. Esbensen, and J.-H. Chu, 1973: Determination of bulk properties of tropical cloud clusters from large-scale heat and moisture budgets. *J. Atmos. Sci.*, **30**, 611–627.

Yussouf, N., E. R. Mansell, L. J. Wicker, D. M. Wheatley, and D. J. Stensrud, 2013: The ensemble Kalman filter analyses and forecasts of the 8 May 2003 Oklahoma City tornadic supercell storm using single-and double-moment microphysics schemes. *Mon. Wea. Rev.*, **141**, 3388–3412.

Zhang, C., and Y. Wang, 2017: Projected future changes of tropical cyclone activity over the western North and South Pacific in a 20-km-mesh regional climate model. *J. Clim.*, **30**, 5923–5941.

Zhang, C., Y. Wang, and K. Hamilton, 2011: Improved representation of boundary layer clouds over the southeast Pacific in ARW-WRF using a modified Tiedtke cumulus parameterization scheme. *Mon. Wea. Rev.*, **139**, 3489–3513.

Zhu, T., and D.-L. Zhang, 2006: Numerical simulation of Hurricane Bonnie (1998). Part II: sensitivity to varying cloud microphysical processes. *J. Atmos. Sci.*, **63**, 109–126.

LIST OF TABLES

TABLE 1. Select WRF model settings and parameterizations.

WRF Model Parameterizations:	**9-km Simulation (Domain 1)**	**3-km Simulation (Domain 2)**	**1-km Simulation (Domain 3)**	
Grid spacing	9 km	3 km	1 km	
Vertical levels (Model top)	50 (10 hPa)	50 (50 hPa)	50 (50 hPa)	
Vortex following (Level)	--	--	Yes (500 hPa)	
Long- and shortwave radiation parameterization	RRTMG	RRTMG	RRTMG	(Iacono et al. 2008)
Land surface model	Noah	Noah	Noah	(Chen and Dudhia 2001)
Surface layer physics	Revised MM5 Monin-Obukhov scheme	Revised MM5 Monin-Obukhov scheme	Revised MM5 Monin-Obukhov scheme	(Jimenez et al. 2012)
Other physics	TC surface fluxes	TC surface fluxes	TC surface fluxes	Donelan Cd + Garratt Ck (Lackmann 2015)
Cumulus parameterization	Tiedtke	--	--	(Zhang et. al 2011)
Microphysics	WSM6, WDM6	WSM6, WDM6	WSM6, WDM6	(Hong and Lim 2006), (Lim and Hong 2010)
Planetary boundary layer	YSU, MYNN3, ACM2	YSU, MYNN3, ACM2	YSU, MYNN3, ACM2	(Hong et al. 2006), (Nakanishi and Niino 2006), (Pleim 2007a,b)

TABLE 2. Percentile threshold values for cell type identification for Hurricane Harvey (2017). The model reflectivity values for the 99.9^{th} percentile, 0–3-km updraft helicity values for the 99.95^{th} percentile, and updraft velocity values for the 99.9^{th} percentile are shown.

WRF Model Runs	Model Reflectivity (dBz)	0–3-km Updraft Helicity (m^2/s^2)	Max Updraft Velocity (m/s)
Harvey (2017):			
WSM6—YSU	52.41	32.95	15.13
WSM6—MYNN3	51.24	21.71	11.17
WSM6—ACM2	53.25	37.85	16.80
WDM6—YSU	51.18	33.64	15.33
WDM6—MYNN3	50.61	21.89	11.31
WDM6—ACM2	51.23	33.92	16.42

TABLE 3. Percentile threshold values for cell type identification for Hurricane Irma (2017). The model reflectivity values for the 99.9^{th} percentile, 0–3-km updraft helicity values for the 99.95^{th} percentile, and updraft velocity values for the 99.9^{th} percentile are shown.

WRF Model Runs	Model Reflectivity (dBz)	0–3-km Updraft Helicity (m^2/s^2)	Max Updraft Velocity (m/s)
Irma (2017):			
WSM6—YSU	54.74	109.48	17.18
WSM6—MYNN3	53.47	57.62	13.51
WSM6—ACM2	55.31	126.32	19.33
WDM6—YSU	52.34	98.45	20.16
WDM6—MYNN3	51.91	65.43	13.98
WDM6—ACM2	52.59	113.50	18.31

LIST OF FIGURES

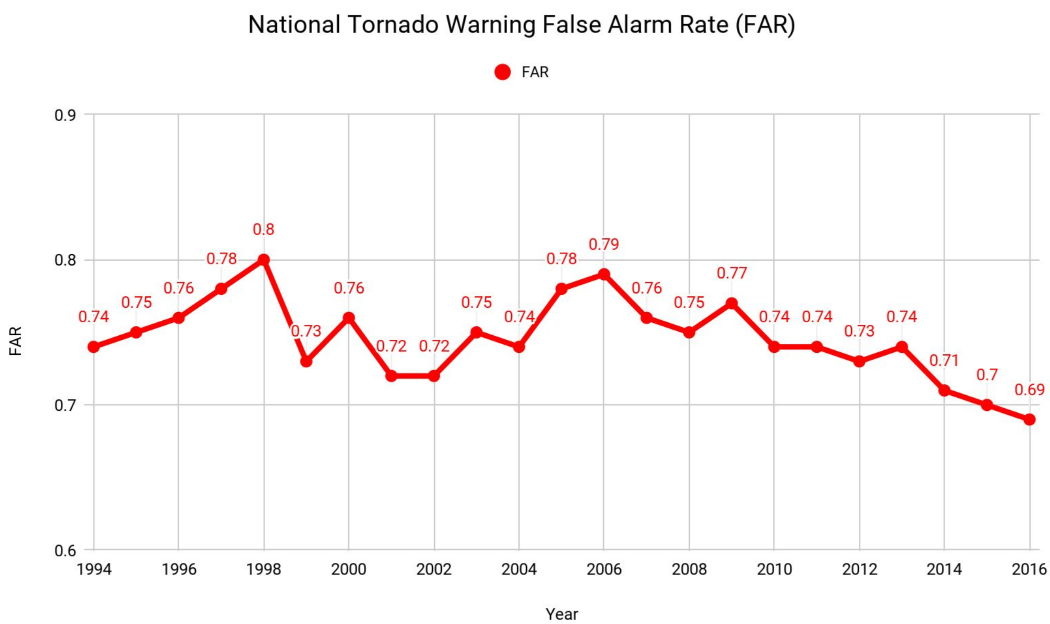

FIG. 1. National tornado warning false alarm ratio (FAR) for the United States from the Storm Prediction Center (SPC) 1994–2016.

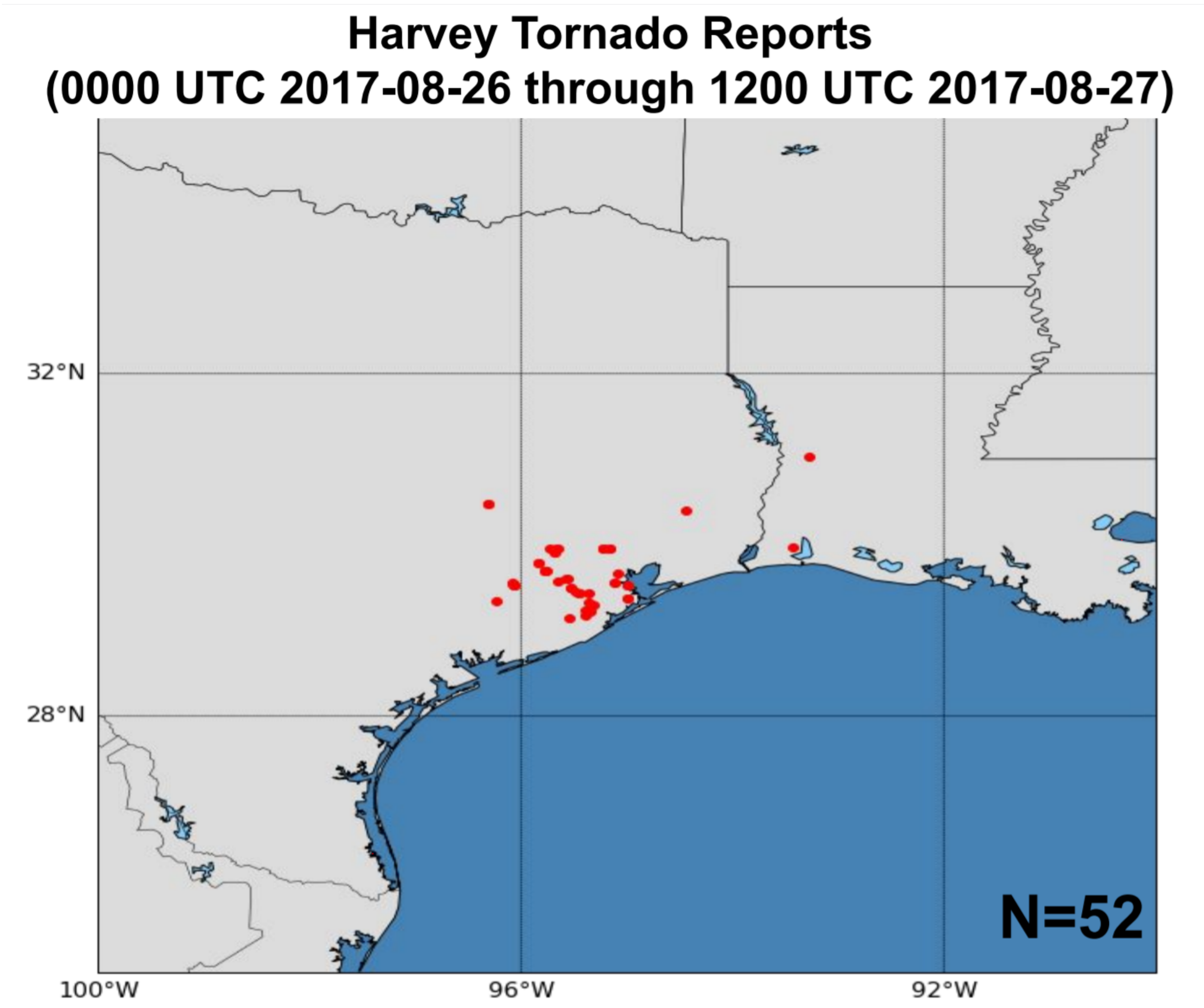

FIG. 2. Storm Prediction Center (SPC) tornado reports (red) for 0000 UTC 26 August through 1200 UTC 27 August.

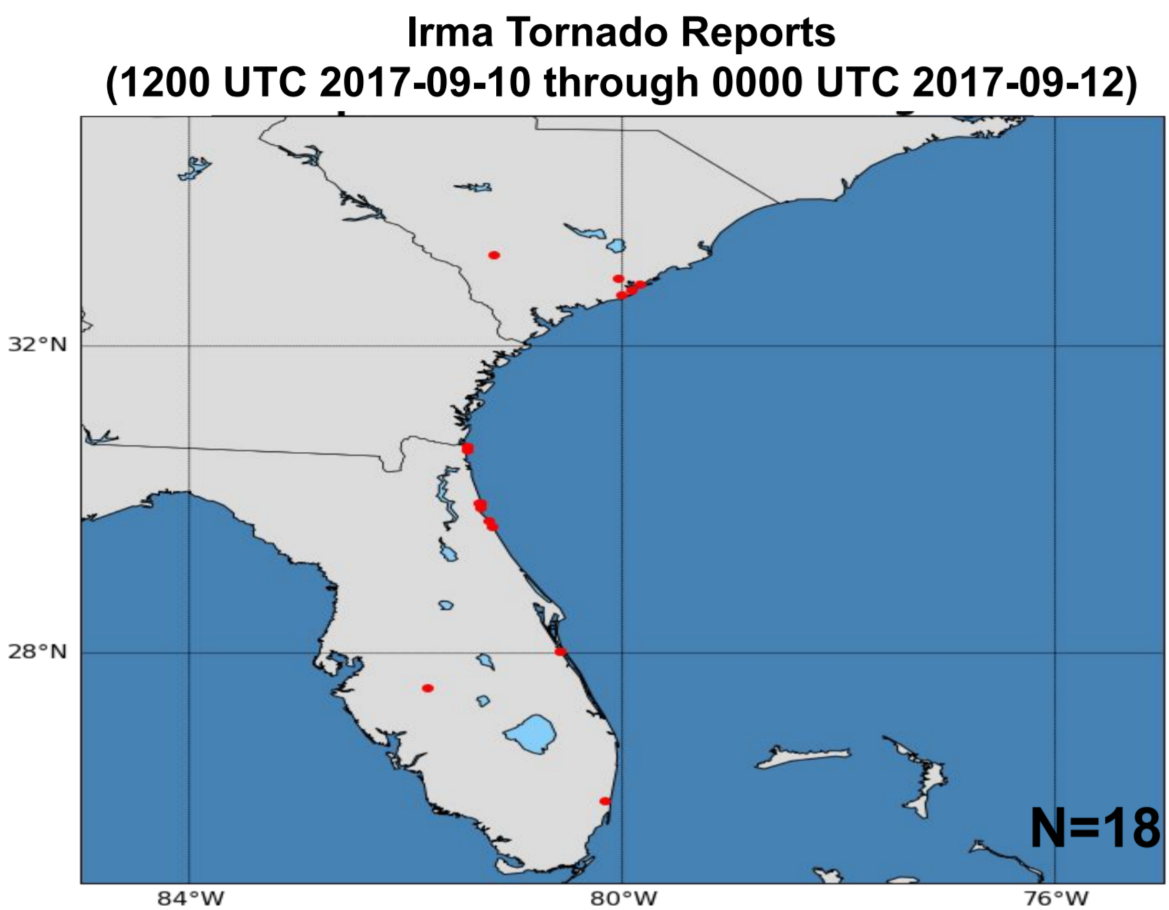

FIG. 3. Storm Prediction Center (SPC) tornado reports (red) for 1200 UTC 10 September through 0000 UTC 12 September.

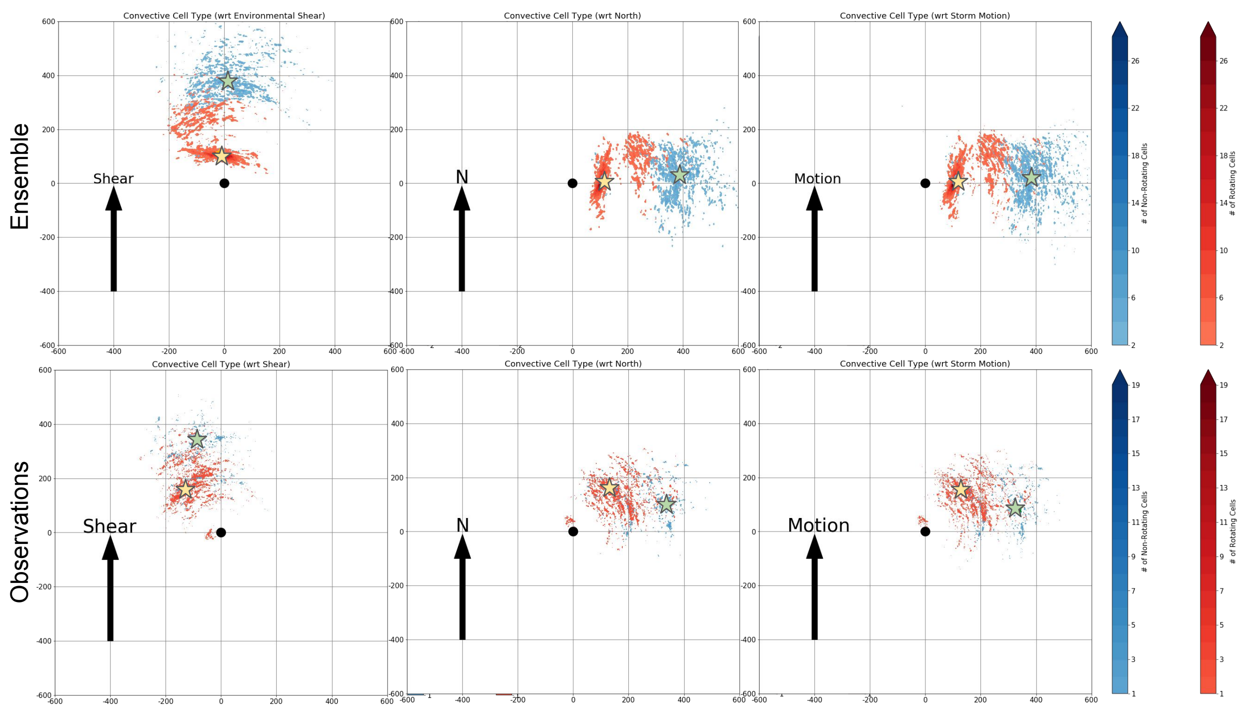

FIG. 4. Distribution of rotating (red) and non-rotating (blue) cells in the NCAR ensemble initialized at 0000 UTC 26 August (top) and observations (bottom) with respect to vertical shear, north, and storm motion from 0000 UTC 26 August through 1200 UTC 27 August 2017. Center of mass of the rotating cells (star yellow) and non-rotating cells (star green). From Card (2019).

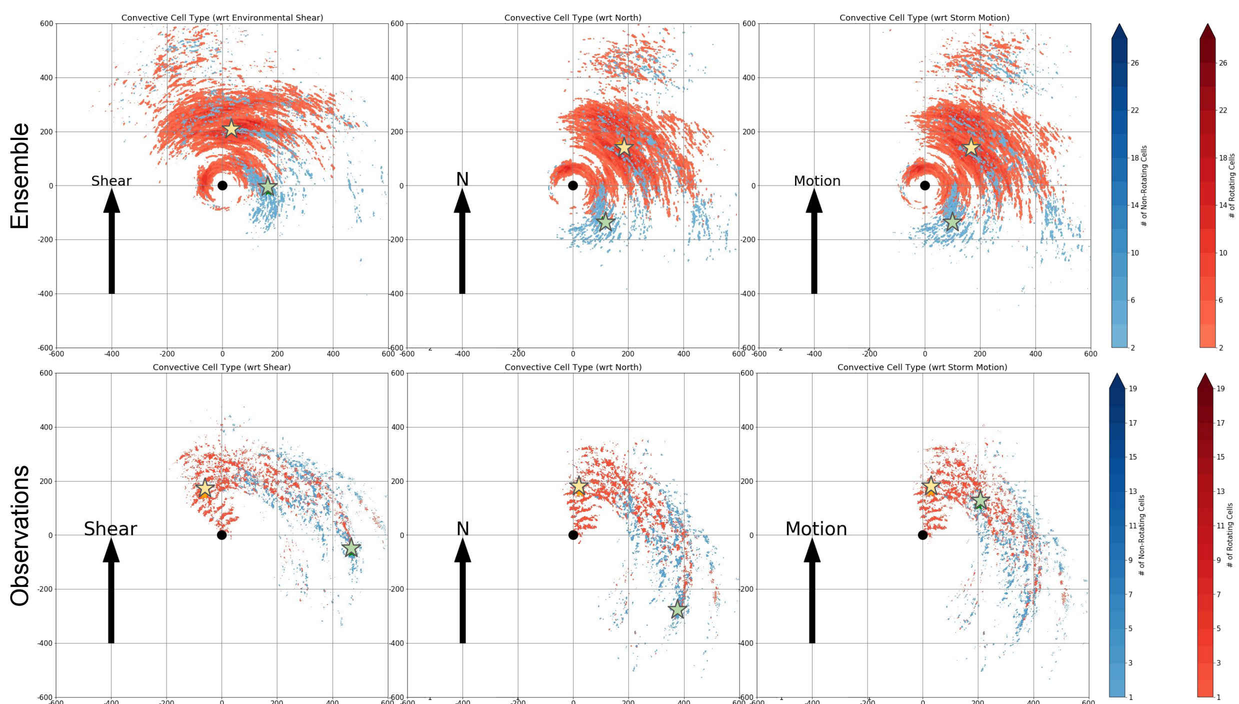

FIG. 5. Same as Figure 4, but for Hurricane Irma (2017) from 1200 UTC 10 September through 0000 UTC 12 September 2017. The NCAR ensemble was initialized at 0000 UTC 10 September. From Card (2019).

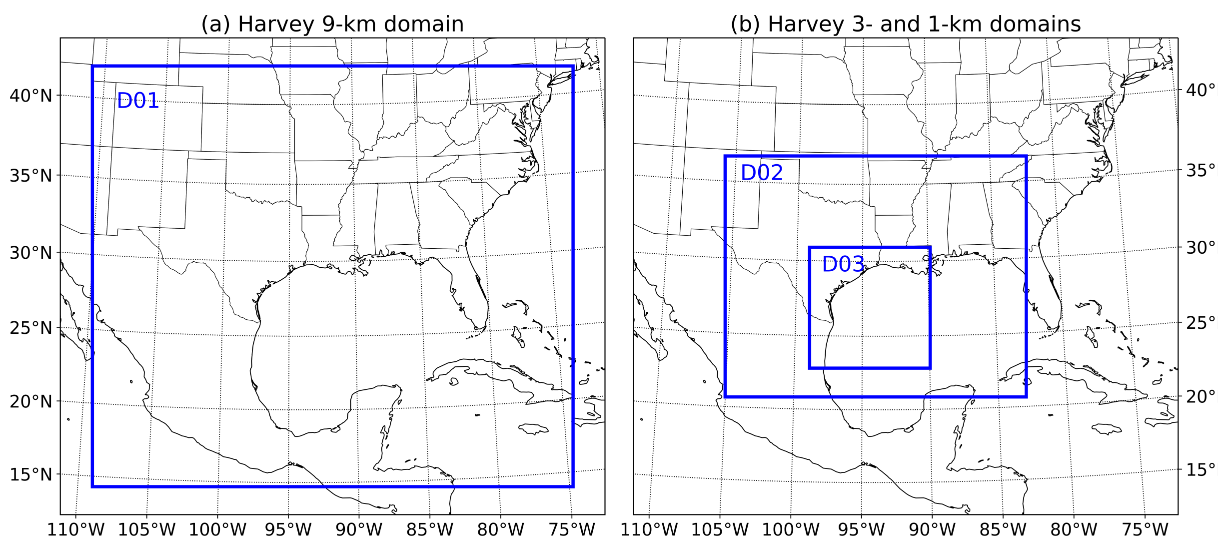

FIG. 6. The WRF domains for Hurricane Harvey (2017): a) 9-km domain (D01, 350 X 300 gridpoints) and b) 3-km static domain (D02, 750 X 600 gridpoints) with 1-km vortex following domain (D03, 901 X 901 gridpoints).

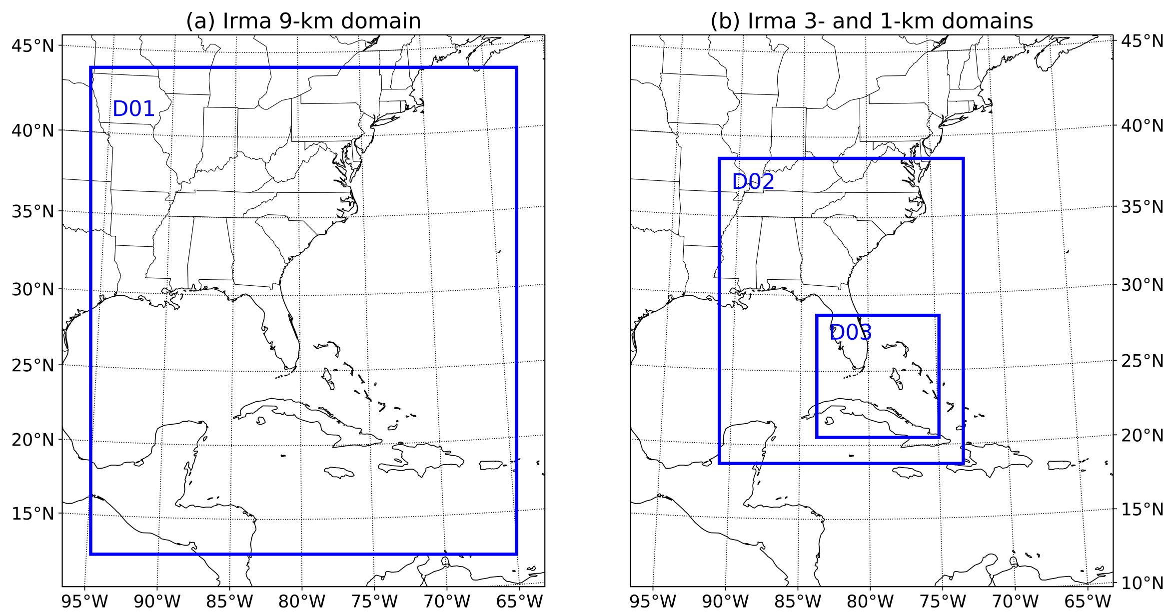

FIG. 7. The WRF domains for Hurricane Irma (2017): a) 9-km domain (D01, 300 X 350 gridpoints) and b) 3-km static domain (D02, 600 X 750 gridpoints) with 1-km vortex following domain (D03, 901 X 901 gridpoints).

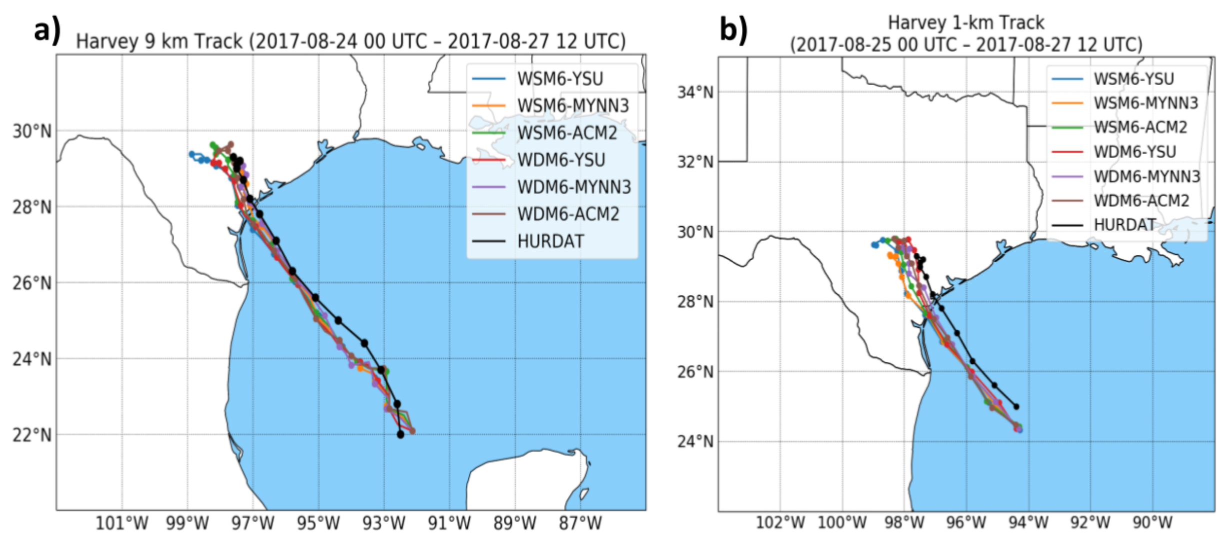

FIG. 8. Tropical cyclone tracks using minimum sea level pressure for the a) 9-km WRF simulation initialized at 0000 UTC 24 August and b) 1-km WRF simulation initialized at 0000 UTC 25 August, compared to the Atlantic Best Track of Hurricane Harvey (2017) every 6 h.

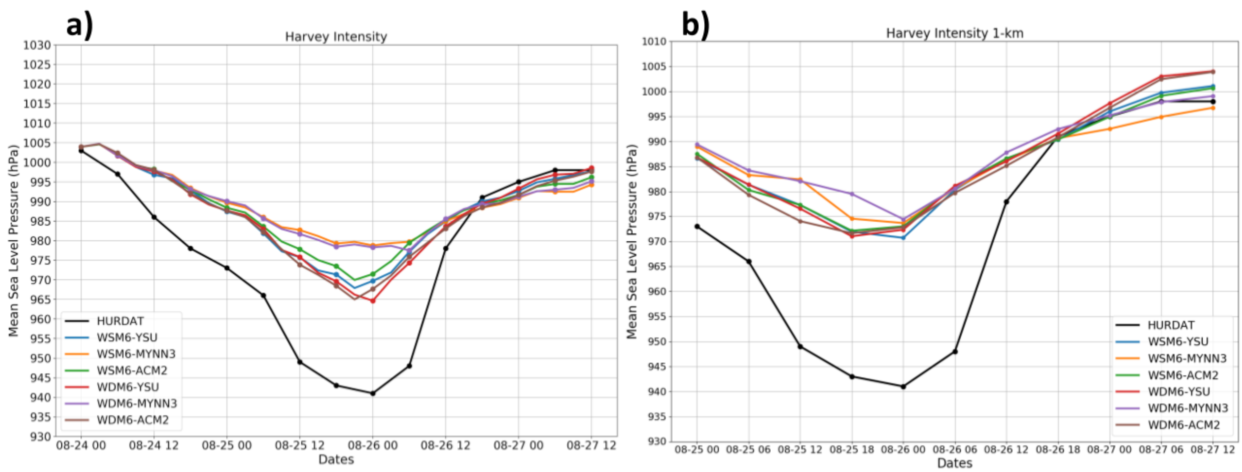

FIG. 9. Intensity, in terms of minimum sea level pressure (hPa), for the a) 9-km WRF simulation initialized at 0000 UTC 24 August and b) 1-km WRF simulation initialized at 0000 UTC 25 August, compared to the Atlantic Best Track of Hurricane Harvey (2017) every 6 h.

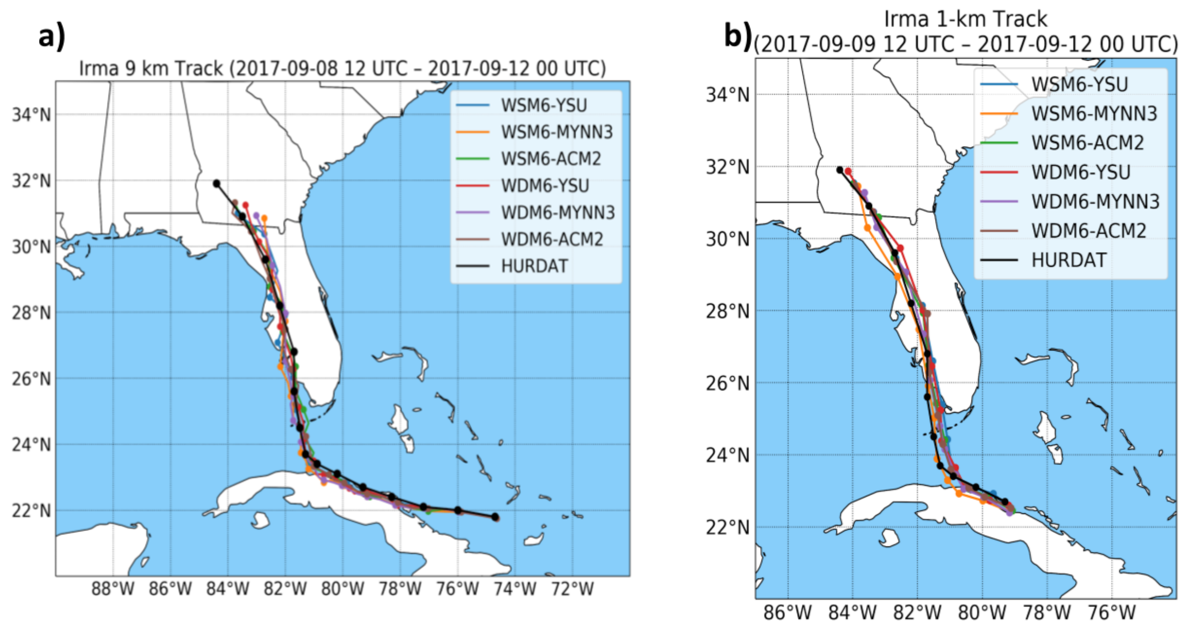

FIG. 10. Tropical cyclone tracks using minimum sea level pressure for the a) 9-km WRF simulation initialized at 1200 UTC 8 September and b) 1-km WRF simulation initialized at 1200 UTC 9 September, compared to the Atlantic Best Track of Hurricane Irma (2017) every 6 h.

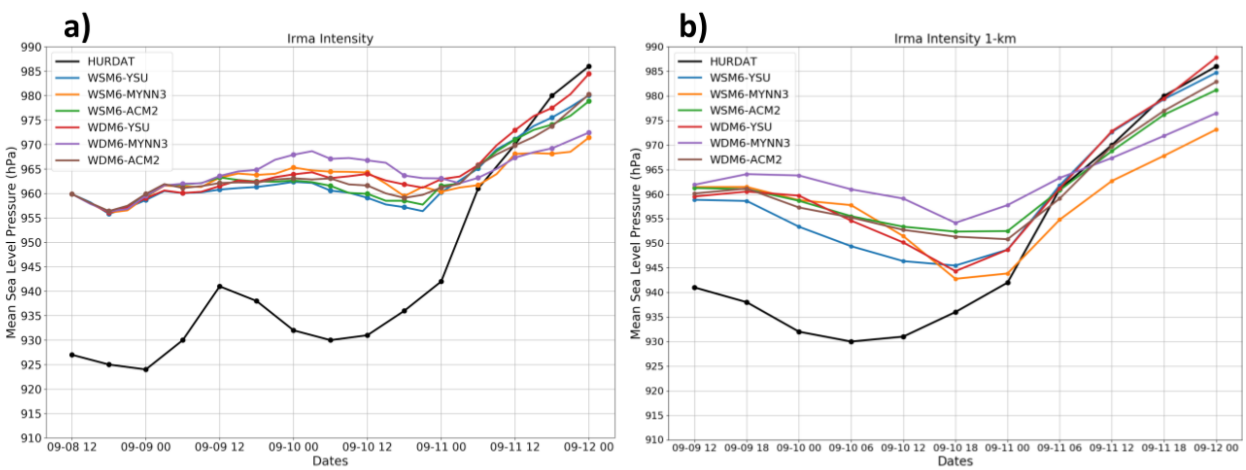

FIG. 11. Intensity, in terms of minimum sea level pressure (hPa), from the a) 9-km WRF simulation initialized at 1200 UTC 8 September and b) 1-km WRF simulation initialized at 1200 UTC 9 September, compared to the Atlantic Best Track of Hurricane Irma (2017) every 6 h.

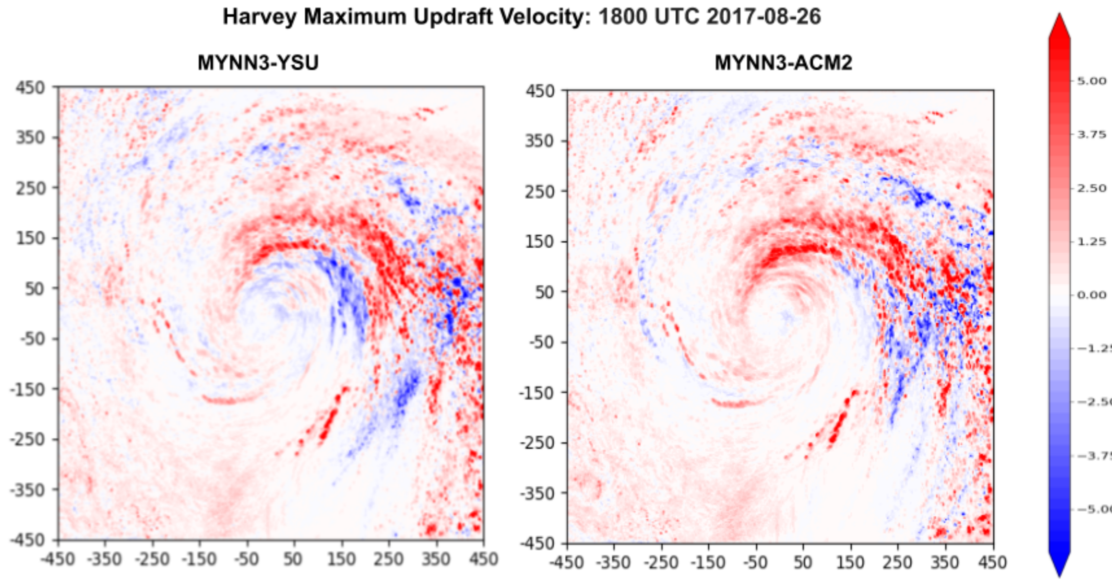

FIG. 12. 0–3-km vertical velocity difference ($m\ s^{-1}$, shaded) for the MYNN3 PBL scheme between the YSU (left) and ACM2 (right) for Hurricane Harvey (2017) at 1800 UTC 26 August.

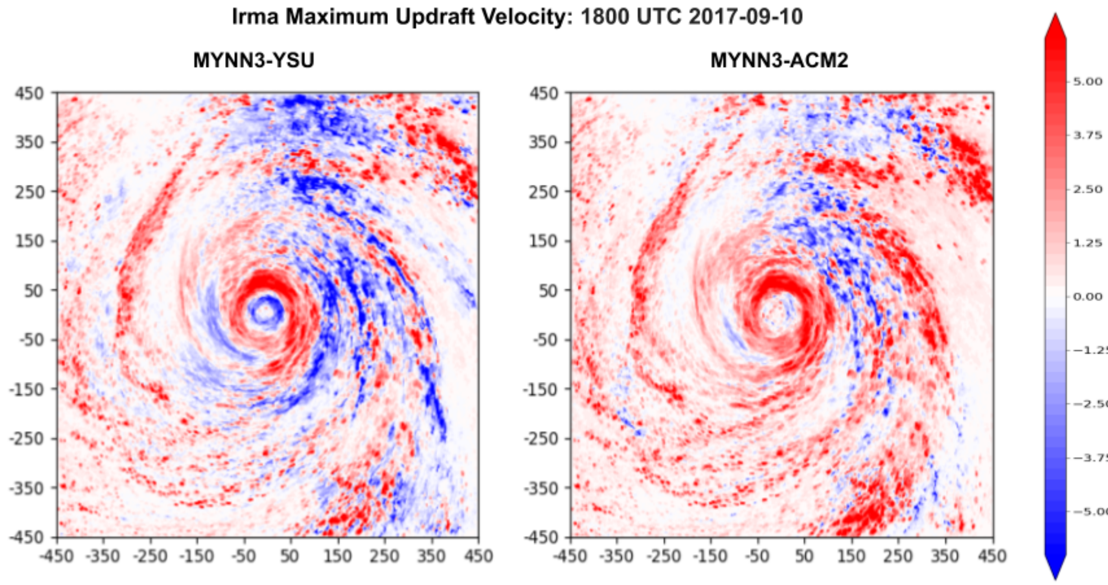

955 FIG. 13. 0–3-km vertical velocity difference ($m\ s^{-1}$, shaded) for the MYNN3 PBL scheme between the YSU
956 (left) and ACM2 (right) for Hurricane Irma (2017) at 1800 UTC 10 September.

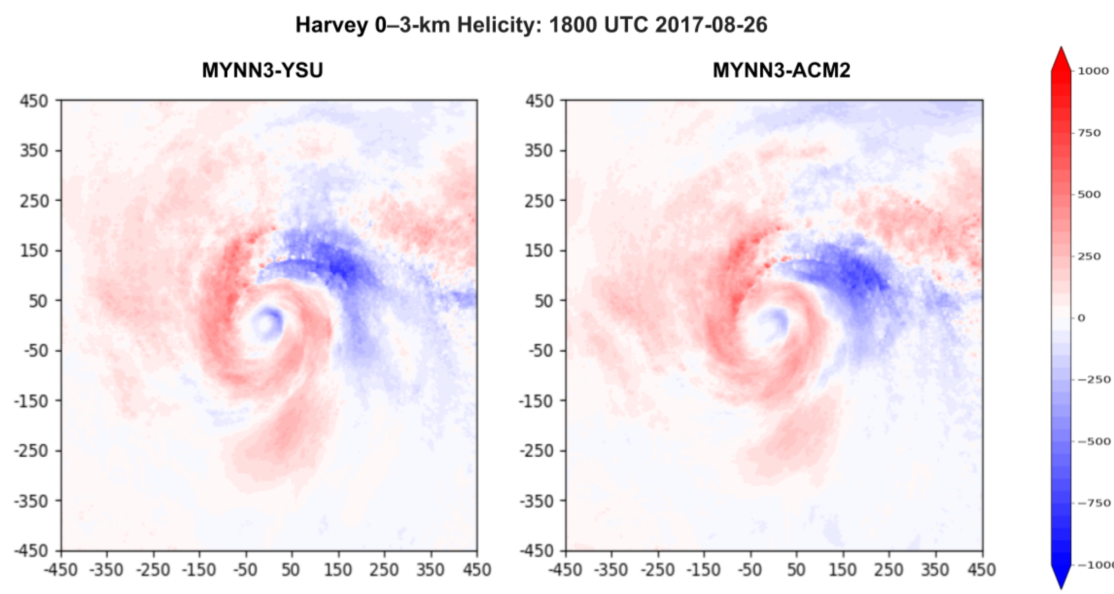

957 FIG. 14. 0–3-km helicity difference (m^2 s^{-2}, shaded) for the MYNN3 PBL scheme between the YSU (left) and ACM2 (right) for Hurricane Harvey (2017) at 1800 UTC 26 August.

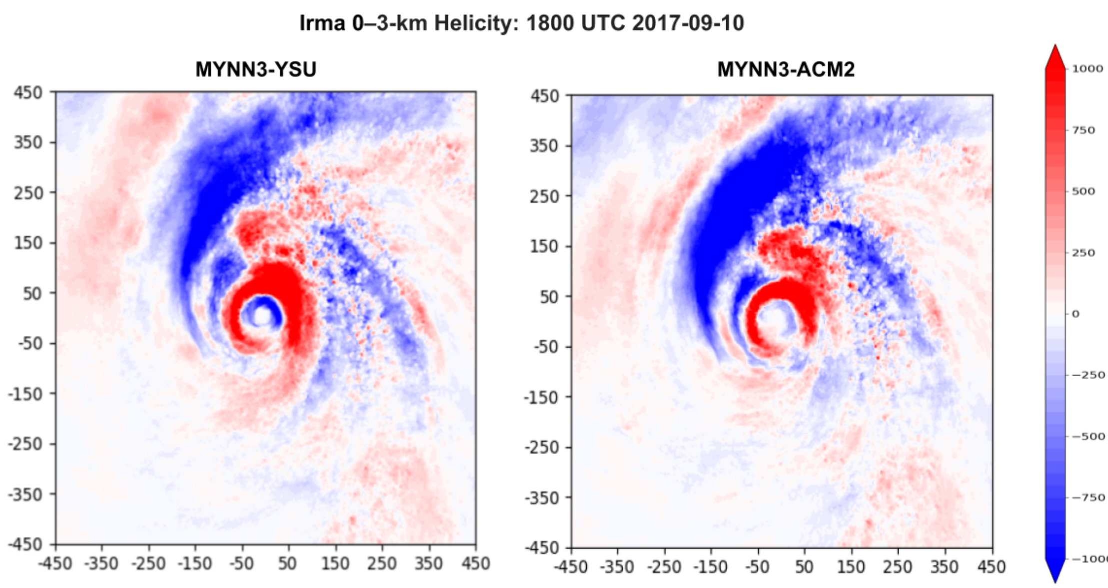

959 FIG. 15. 0–3-km helicity difference (m^2 s^{-2}, shaded) for the MYNN3 PBL scheme between the YSU (left)
960 and ACM2 (right) for Hurricane Irma (2017) at 1800 UTC 10 September.

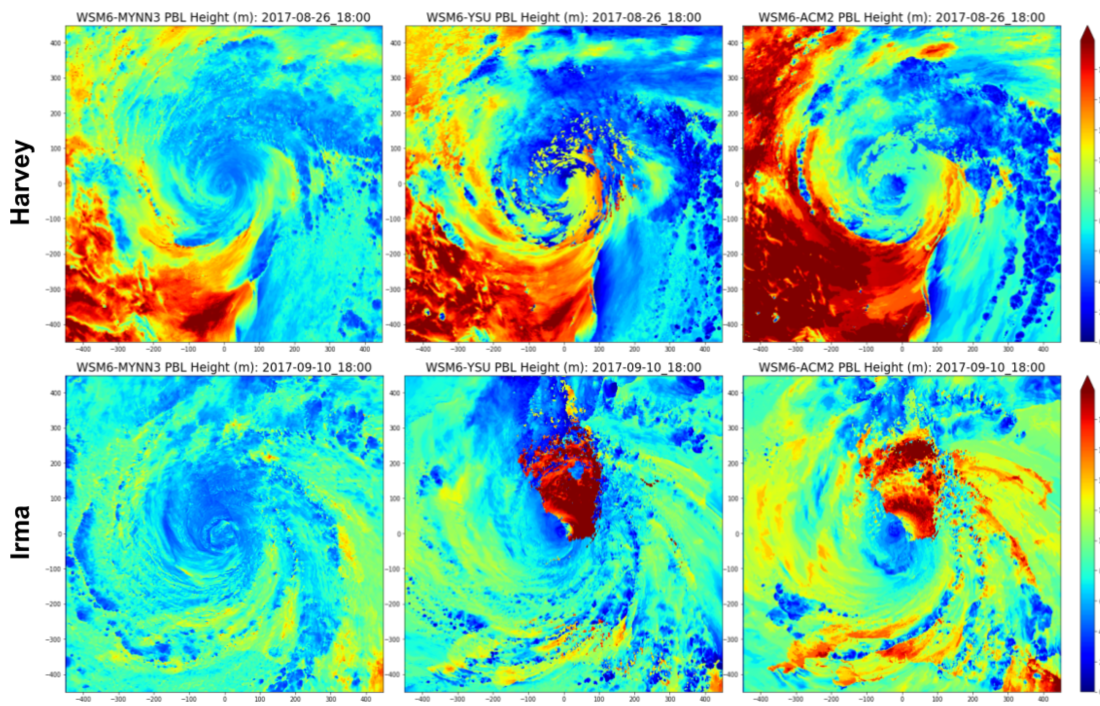

FIG. 16. Planetary boundary layer height (m, shaded) for the MYNN3, YSU, and ACM2 PBL schemes in hurricanes Harvey (top) and Irma (bottom) (2017) at 1800 UTC 26 August and 1800 UTC 10 September, respectively.

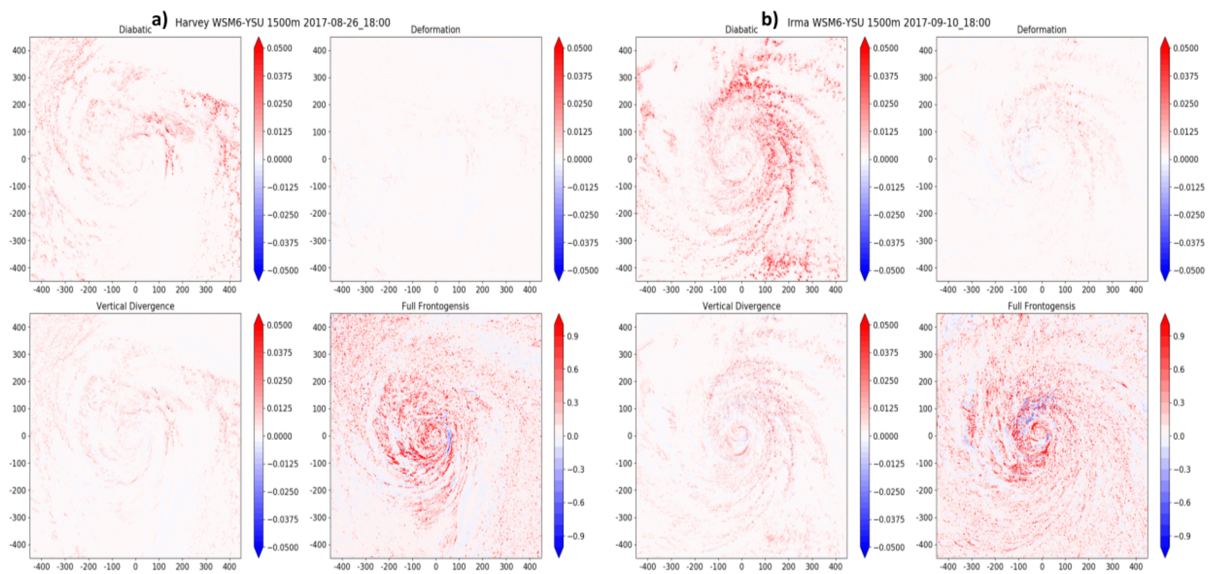

FIG. 17. WSM6–YSU simulation 1500-m diabatic, deformation, vertical divergence, and the full frontogenesis equations ($\frac{K}{skm}$, shaded) at a) 1800 UTC 26 August for Hurricane Harvey (2017) and b) at 1800 UTC 10 September for Hurricane Irma (2017).

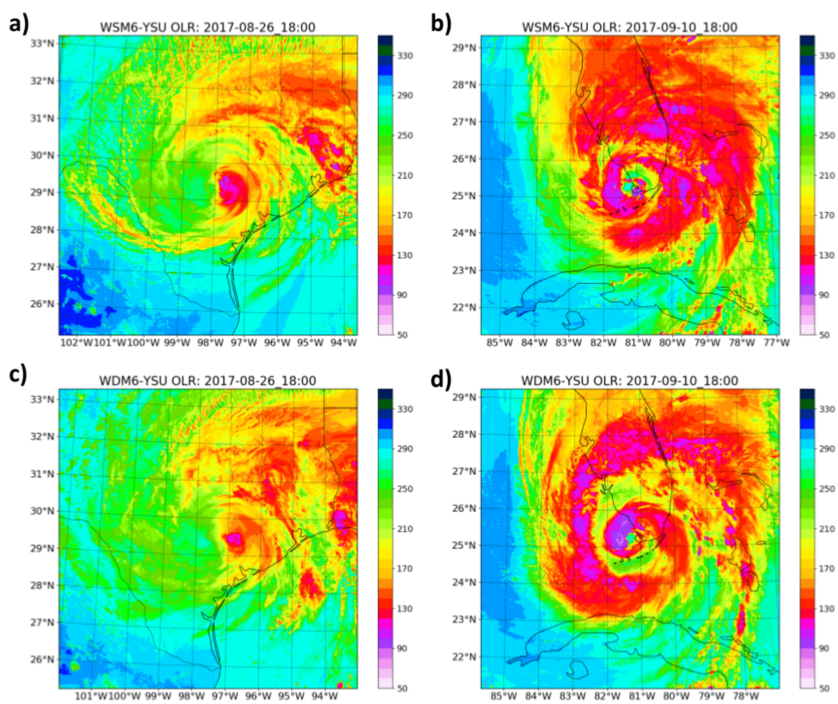

967 FIG. 18. Outgoing longwave radiation (K, shaded) for the a) WSM6 and c) WDM6 simulations for 1800 UTC 26 August for Hurricane Harvey (2017) and b) WSM6 and d) WDM6 simulations at 1800 UTC 10 September for Hurricane Irma (2017).

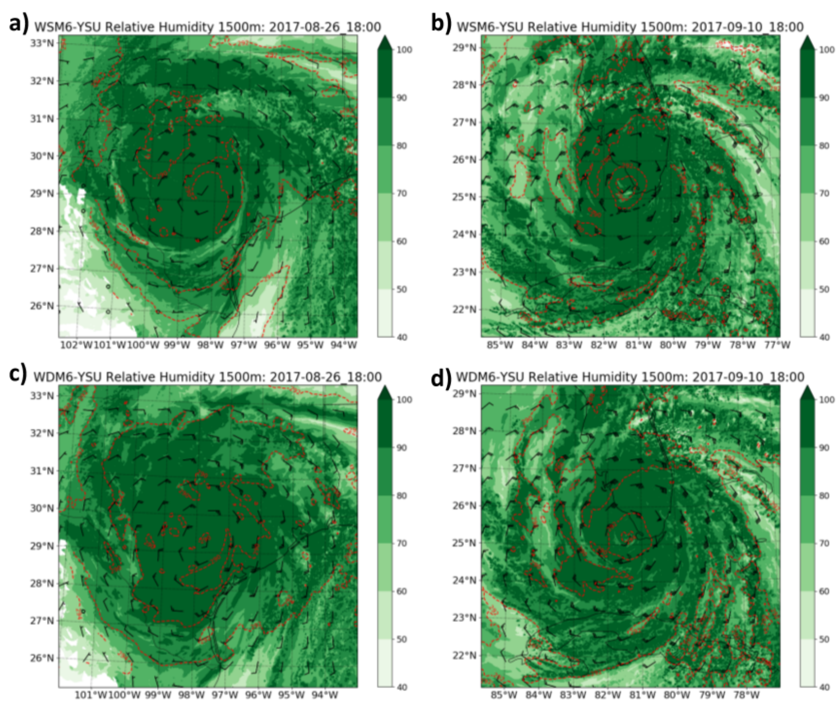

FIG. 19. 1500-m relative humidity (%, shaded), potential temperature (K, dashed), and wind barbs ($m\ s^{-1}$, standard convention) for the a) WSM6 and c) WDM6 simulations for 1800 UTC 26 August for Hurricane Harvey (2017) and b) WSM6 and d) WDM6 simulations at 1800 UTC 10 September for Hurricane Irma (2017).